Experimental Measurement of Air-Water Capillary Pressure Curves at Elevated Temperatures

By

Kiran Prasad Shrestha

McGill University, Montreal

A Thesis

Submitted To McGill University

In Partial Fulfillment of the

Requirements of the Degree of

Master of Engineering

In

Chemical Engineering

Acknowledgements

Abstract

A capillary pressure curves provides important information about the porous system such as porosity, breakthrough pressure, fluid–solid wettability and capillary hysteresis. The measurement of capillary pressure curves is one of the most commonly adopted methods of measuring wettability in a porous system. However, to date these measurements are done only at room temperature because of the limitations of utilising existing equipment at higher temperatures. The capillary behaviour of liquid in porous system can be a different when subjected to harsh condition such as high temperature and pressure. An experimental setup has been designed and developed to measure air-water capillary pressure curves for gas diffusion layers (GDLs) used in polymer electrolyte membrane fuel cells at elevated temperatures. Experiments were conducted at various temperatures in the direction of increasing and decreasing temperatures for Toray 120 and Toray090 with varying PTFE loadings. Notable shifts in the capillary behavior were seen and in some cases the shifts were of the same size as PTFE addition. In untreated samples the results suggest that GDL wettability changes with temperature once the temperature dependence of the surface tension has been accounted for. In treated samples, however, the wettability remains more or less constant with temperature. This behavior is in agreement with the temperature dependent values of water contact angle on PTFE and graphite. Observed shift with temperature for treated samples are more or less reversible during decreasing temperature.

Abstrait

A courbes de pression capillaire fournit des informations importantes sur le système poreux tels que la porosité, la pression de fuite, le liquide-solide mouillabilité et l'hystérésis capillaire. La mesure des courbes de pression capillaire est une des méthodes les plus couramment adoptée pour mesurer la mouillabilité dans un système poreux. Cependant, à ce jour, ces mesures sont effectuées uniquement à la température ambiante en raison des limitations de l'utilisation des équipements existants à des températures élevées. Le comportement capillaire de liquide dans le système poreux peut être un différent lorsqu'elle est soumise à l'état dur, comme la température et une pression élevées. Un dispositif expérimental a été conçu et développé pour mesurer air-eau courbes de pression capillaire pour les couches de diffusion de gaz (GDL) utilisés dans les cellules à électrolyte polymère à combustible à membrane à des températures élevées. Expériences ont été réalisées à différentes températures dans le sens d'une augmentation et la diminution des températures de Toray120 et Toray090 avec différents chargements PTFE. Changements notables dans le comportement capillaire ont été observées et, dans certains cas, les changements étaient de la même taille que l'addition de PTFE. Dans les échantillons non traités les résultats suggèrent que les changements de mouillabilité GDL avec la température une fois que la dépendance en température de la tension de surface a été pris en compte. Dans les échantillons traités, cependant, la mouillabilité reste plus ou moins constant avec la température. Ce comportement est en accord avec les valeurs dépendantes de la température de l'angle de contact de l'eau de PTFE et de graphite. Décalage observé avec la température pour les échantillons traités sont plus ou moins réversible pendant la température diminue.

Table of Contents

List of Figures

1.   Introduction

1.1.   Motivation

Polymer electrolyte membrane fuel cells (PEMFCs) are being considered as power sources for various applications because of their high power density compared to other power generation technologies. They are a key component in a renewable energy economy, since hydrogen can be used to store energy generated by intermittent renewable sources. All of the major car companies are pursuing hydrogen fuel cells to replace internal combustion engines, but several technical challenges must be addressed before fuel cells can be mass produced and commercialized. Accumulation of liquid water in the porous electrode components and the general problem of water management in PEMFCs continue to be a major problem. At higher current densities, the water production rate in the cathode is high and can exceed the removal rate. This results in water accumulation, causing flooding and hindering the gas phase transport of oxygen by clogging the pores in the porous electrode, leading to lower operating efficiency. As a result, more cells are required in a fuel cell stack to produce a given power density which in turn results in high cost. Hence, understanding the multiphase flow conditions and their impact on transport processes remains a vital task.

A number of recent studies have explored the wettability characteristics of the porous electrode by measuring air-water capillary pressure-saturation curves [1-5]. Accurate knowledge of the capillary pressure curves is essential for two main reasons. Firstly, it provides a means to quantify the wettability and water behavior in these materials. This information is used to gather practical information such as evaluating the impact of different porous structures and wettability altering coatings on water behavior, as well as the fundamental study of water configurations and percolation conditions in the electrodes. The second key role of these experiments is to provide constitutive relationships to complex "multiphysics" models of fuel cell operation. Computer modeling of the many coupled transport processes, including multiphase flow conditions, is one main tool used by fuel cell researchers to understand the factors that impact cell performance. Since multiphase flow and water flooding are so critical to fuel cell performance at high current density, it is imperative to have accurate capillary

1

pressure data to supply to these models. Virtually all the previous studies in this area have been conducted at room temperature, yet fuel cells operate above 80°C. The present work focuses on developing a capillary pressure test able to study samples at elevated temperatures to more fully understand the wettability of GDL electrodes at fuel cell operating conditions.

1.2. Hypothesis

The impact of elevated temperature on capillary properties in porous materials is commonly studied by petroleum recovery and aquifer researchers to account for geothermal effects [6, 7]. Although a fairly large amount of work has been done in these disciplines, tests are usually done directly on soil or rock core samples which contain impurities found in the natural environment. In these cases, the dissolution or leaching of impurities into the liquid phase at increased temperatures has a large effect on wettability and surface tension of the system. Those findings do not translate to fuel cell electrodes, however, which contain pure air and water with almost no impurities. A limited amount of previous work on pure systems such as air-water-glass beads and sandstone found that capillary pressure curves shifted to smaller values as temperature increased[7, 8]. This is not unexpected since capillary pressure ($P_C = P_L - P_G$) is proportional to the surface tension (σ) of the air-water system as given by the Young-Laplace equation ($P_C = 2\sigma H$), and σ decreases with increasing temperature from 0.072 N/m at 25°C to just under 0.06 N/m at 100°C. She and Sleep[8], however, found that the capillary pressure shifted more than could be explained by the surface tension effect alone, indicating that other factors may also be involved, such as changing wettability.

The expectation that changing wettability may be the reason for the observed shifts in capillary pressure curves is based on the commonly used solution of the Young-Laplace equation for cylindrical capillaries proposed by Washburn[9]:

$$P_C = \left(2\sigma\right)\left(-\cos\theta\right)\left(r^{-1}\right)$$

(1)

Where r is the radius of the cylindrical pore and θ is the contact angle measured through the liquid phase of a liquid droplet on a flat surface of the solid (wetting angle or contact angle is discussed in more detail in Section 3.3). Though Eq.(1) is not strictly valid for complex geometries [10], it does give some qualitative insight into the role of temperature on capillary

pressure. For instance, since $\sigma = f(T)$ is known, its impact on capillary pressure can be accounted for by dividing Eq.(1)by σ. Since pore radius does not change with temperature (neglecting thermal expansion of the material) any shifts in P_C/σ can be attributed, at least qualitatively, to changes in wettability owing to the $-cos\theta$ term. Evidence given by Lim and Wang [11] showed that GDL wetting angle θ of carbon paper treated with 10-40% FEP (fluorinated ethylene propylene)did indeed decrease from 108° to 80° with increasing temperature from 25°C to 80°C. It is therefore reasonable to expect that GDL capillary pressure curves, once corrected for surface tension changes, might also shift due to changes in wettability. This hypothesis is further supported by considering Young's equation, which relates the wetting angle to all the interfacial surface tensions in the system[9]:

$$-\cos\theta = \frac{\sigma_{SG} - \sigma_{SL}}{\sigma_{LG}}$$

(2)

Where σ_{SG} is the solid-gas surface tension, σ_{SL} is the solid-liquid surface tension and σ_{LG} is the familiar gas-liquid surface tension, σ. Since σ changes with temperature then this quotient will remain constant only if the other (less well known) surface tension values change together in just the right way, which seems unlikely.

The above considerations are only qualitative however, so experimental determination of water-air capillary pressure curves as a function of temperature is required. Measuring GDL capillary pressure curves at elevated temperatures using the established methods is challenging since they all employ sensitive analytical balances and syringe pumps. In this work, a new experimental setup has been designed and built to measure capillary pressure curves at temperatures as high as 90°C. The entire device is placed inside an oven which controls the system temperature. Experiments have been conducted at various temperatures using one commonly used electrode material with various wettability-altering coatings.

1.3. Objectives

The three main objectives of this work are as follows:

- To design and build an experimental setup that is able to measure capillary pressure curves of GDL materials at elevated temperatures.

- To measure capillary pressure curves for a variety of GDL electrodes materials with varying wettability altering treatments at increasing and decreasing temperatures.
- To assess how much, if any, of the observed changes in capillary pressure behavior are due to changes in wettability of the materials.

2. Background

The invention of the fuel cell as an energy conversion system is attributed to Sir William Grove and Christian Friedrich Schonbein during 19th Century[12]. Despite this early start they have remained largely undeveloped during their first century as primary power sources. The advent of modern materials science techniques (e.g. carbon supported platinum nano particle catalysts) and polymer processing (e.g. ion conducting membranes) techniques has made fuel cells economically and technically feasible. In the past 15 years there has been a massive effort to bring this technology to maturity and begin commercialization.

The environmental consequences of using fossil fuels for vehicles propulsion have become a major contributing factor to the development of fuel cell technologies. The growing dependence of industrialized countries on fossil fuels has had a major impact on oil prices. Current oil reserves will not be able to sustain this ever-increasing demand. Moreover, growing awareness of climate change and the need for sustainable energy alternatives has accelerated. Therefore renewable energy sources like wind and solar will become increasingly important. Due to their irregular availability, these sources are not suited to cover the same electrical base load as natural gas and coal fired power plants. However, these could be utilised in the future to produce hydrogen for use in fuel cells, thus enabling the large scale storage of electricity.

It is because of their high power density that the PEM fuel cells have gained a considerable amount of attention in automobile industries. The modern PEM fuel cell is able to match the internal combustion engine in terms of both power density (horsepower) and energy density (range). Fuel cell commercialization has been delayed by unexpected durability and reliability issues, but these have been largely solved. At present the main limiting factor is high cost. A large amount of research has attempted to reduce cost by lowering the platinum loading in catalysts [13] and exploring inexpensive materials and construction methods[14]. The currently favored target for cost reduction is to increase power density and thereby reduce cell size and component cost. This approach, however, leads to problems with electrode and cell water flooding, since the water produced as the product of the oxygen reduction reaction must be

removed from the cell as rapidly as it's produced to prevent accumulation in the porous electrodes, which creates numerous difficulties.
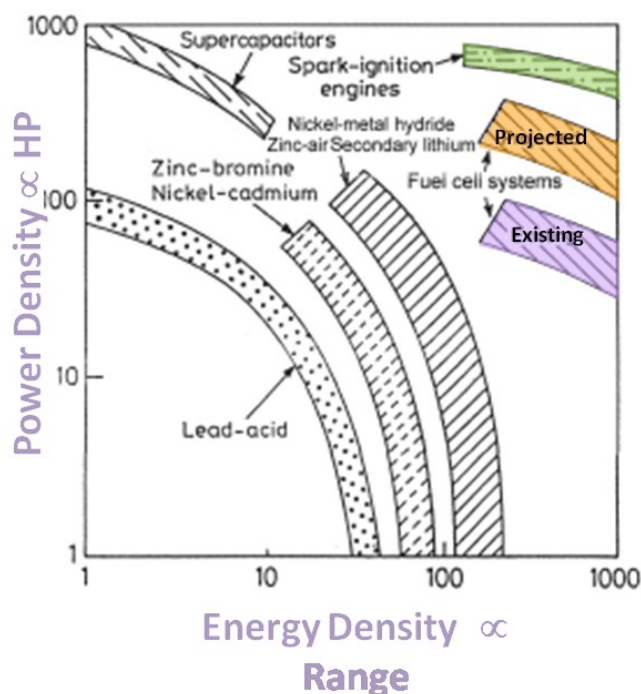
Figure 1: Comparison of electrical system efficiencies between Fuel cell and other conventional energy conversion systems.

2.1. Electrochemistry

A fuel cell is a galvanic cell which converts chemical energy directly into electrical energy. Reactants are fed continuously and reactions occur at catalyst layers, as shown in Figure 2. At the anode, hydrogen gas is fed continuously where it diffuses through the gas diffusion layer and reaches the platinum electrode surface. The hydrogen oxidation reaction takes place at the platinum catalyst surface and hydrogen molecules splits into protons and electrons:

$$2H_2 \rightarrow 4H^+ + 4e^-$$

(3)

At the cathode electrode, protons that have permeated through the ionically conductive membrane combine with oxygen and electrons on platinum particles to form water:

$$O_2 + 4H^+ + 4e^- \rightarrow 2H_2O$$

(4)

The overall reaction occurs as follows:

$$2H_2 + O_2 \rightarrow 2H_2O$$

(5)
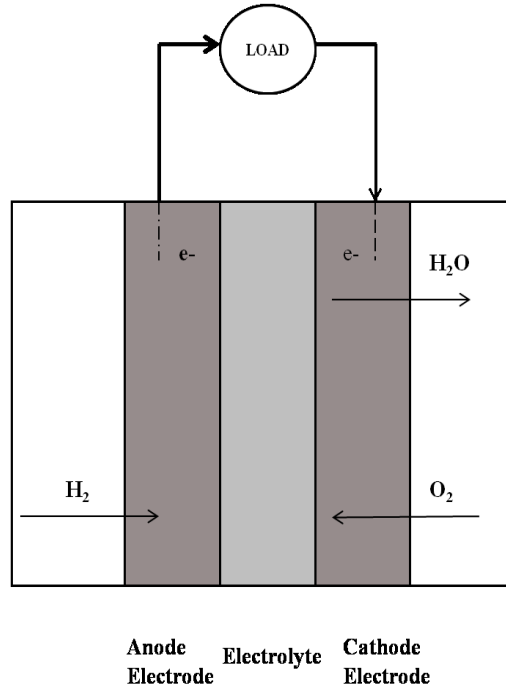
Figure 2: Galvanic cell representation of PEM fuel cell.

2.2. Operating Principles of a Fuel Cell

At open circuit, when no current is flowing, a fuel cell provides the maximum voltage corresponding to the electrochemical potential of the two half reactions governed by Eq.(3) and Eq.(4)which is about 1.223 V. In an ideal reversible fuel cell, voltage is independent of the current drawn. However perfect reversibility cannot be achieved in practice and the theoretical cell voltage is not achieved during operation. The difference in the cell voltage at a given current density (current per unit active electrode area) and ideal cell voltage is called "cell overvoltage" or over potential. Dominant sources of overvoltage in fuel cells include:

a) Mixed Potential: These arise due to unfavorable parasitic reactions that occur on the surface of anodes and cathodes, and which tend to lower the equilibrium electrode potential. One

important reason that mixed potential occurs is the cross-over of fuel through the electrolyte from anode to cathode, and vice-versa.

b) Activation Losses: These are due to slow kinetics at the electrodes. The effects of these types of losses are more obvious at low current densities. For example slow oxygen reduction kinetics, electron transfer, adsorption and desorption and the formation of intermediates, etc.

c) Ohmic Losses: These are predominantly due to the resistive losses in the protons traveling in the polymer electrolyte material. These types of losses increase proportionally with current density. These losses can be reduced by using thinner and more conductive membrane materials. In a PEMFC these losses are worst when the membrane is dry since the ionic conductivity drops severely [15].

d) Mass transfer losses: These are due to hindered diffusion of reactant species to the electrode surfaces. The effects of these losses are more pronounced at higher current densities since diffusion rates cannot supply the reaction fast enough.

The combined effects of these over-voltages cause the cell voltage output to decrease with increasing current densities. A plot of cell voltage versus current densities is called a polarization curve. A typical polarization curve for a PEM fuel cell is shown in Figure 3.The goal of catalyst development is to reduce the voltage loss seen in the 0 to 0.2 A range. The goal of improving the proton conducting membrane is to reduce the slope seen in the 0.2 to 2.0 range, and the goal of improving mass transfer is to extend the drop seen at 2.0 A to higher currents. All these efforts combine to shift the polarization curve up so operation can occur in the upper right corner of the graph, which yields the highest power per unit area or volume of cell. The power density curve in Figure 3 (dashed line) displays a peak at about 0.8 A/cm^2. The objective of fuel cell companies is to produce a cell that peaks at 3 A/cm^2 and maintains a voltage above 0.65 V.
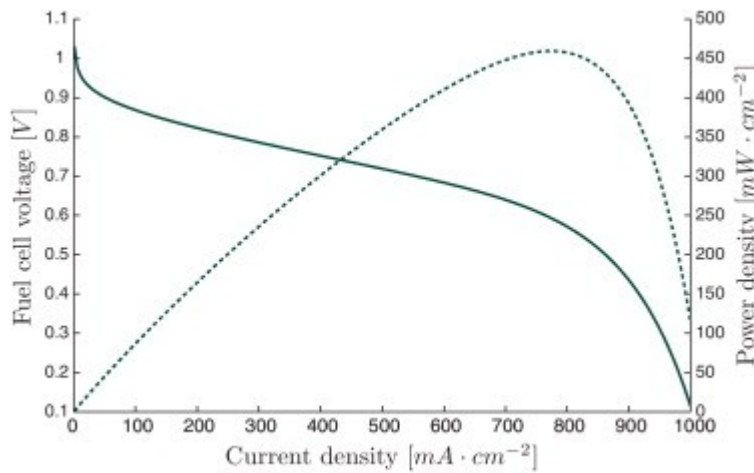
Figure 3: Polarization curves in PEM fuel cell.[16]

2.3. Internal Components of the PEM Fuel Cell

Aschematic diagram of a PEM fuel cell stack is as shown in Figure 4. A stack is made up of several hundred individual cells in series which combine to create a sufficiently high voltage (recall that each cell produces less that 1 V at realistic operating conditions). A single PEM fuel cell consists of a proton conducting polymeric membrane sandwiched between an anode and cathode electrode assemblies. The electrolytic membrane is a thin, gas impermeable polymeric membrane which acts as an ionic conductor to conduct proton generated at anode towards cathode. In order to catalyze the reaction, platinum catalyst particles are applied on either side of the membrane to create a porous film or coating called the catalyst layer. The gas diffusion layer is a fibrous paper material whose main role is to act as a spacer between the flow channels and the catalyst layer, allowing gaseous reactants to reach the catalyst particles lying underneath the ribs and allowing electrons to reach catalyst located over the channels. The fibers of the GDL are generally graphite since it must also act as an electron and heat conductor. Hydrogen gas is supplied at the anode and splits into protons and electrons at the platinum catalyst particles that are applied to the membrane. The protons pass across the polymeric membrane to the cathode while the electrons move through an external circuit in order to produce electricity. Oxygen (in the form of air) is supplied to the cathode and combines with the hydrogen ions to produce water. The bipolar plates provide the gas

9

channels. The reactant gases flow through the channels and diffuse to the reaction catalysts through GDL, thus mass transfer in the GDL is a major factor in cell operation.
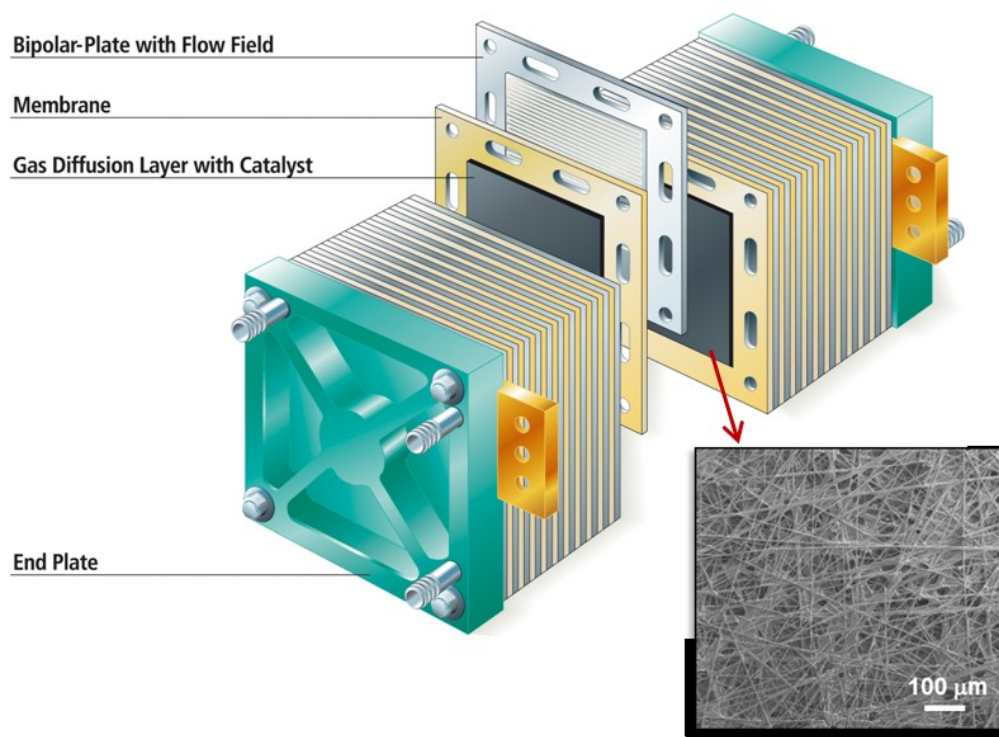
Figure 4: Internal components of a PEMFC stack.

2.4. Water Management in PEMFC

Water management in PEMFCs is a challenge because they do not operate well when too wet or when too dry. The operating temperature of a typical PEM fuel cell is below 100°C to prevent excessive evaporation of water and the drying of the membrane. The protonic conductivity of the membrane increases significantly with higher humidity, so maintaining water in the cell is preferred in this regard. On the other hand, too much water inside the cell leads to condensation, resulting in poor gas phase diffusion of reactants. Water vapor is supplied to the fuel cell by humidified reactant gases or by direct liquid hydration[17]. Of course water is also generated inside the cell by the cathode reaction.

Maintaining the correct balance of water inside the cell has been one of the most widely studied issues in the field of PEMFC. Part of the difficulty with water management is that water

transfers throughout the cell through many different processes, depending on the operating conditions. Water transport occurs through the membrane between an anode and a cathode by 1) electro-osmotic drag 2) back-diffusion and 3) convection[18]. Electro-osmotic transport is responsible for driving the water from an anode to the cathode along with the protons [19], back diffusion is caused by the anode being somewhat drier than the cathode and convection is due to the pressure gradient along the fuel cell, though the latter is usually negligible. Water is generated at the cathode and this must be transported away from the catalyst layer by evaporation, water-vapour diffusion and the capillary transport of GDL into the flow channel, and then exhausted at the outlet. If this doesn't happen, excess water accumulates at the cathode side and condenses, thus blocking the pores of GDL and reducing gas transport to the catalyst layer. This is known as "flooding", and is a crucial limiting factor for PEMFC performance. Generally, the flooding of the GDL is linked with high current density operation, because at higher current densities the rate of water production is higher than its removal. However, flooding can also occur even at lower current densities under certain operating conditions, such as low gas temperature and low gas flow rates, where a faster saturation of gas phase by water-vapour can occur [20]. Therefore, water management is a critical factor to consider for maximizing the performances of PEMFC.

One of the main ways of improving water management is to make the porous electrode components more tolerant of liquid water. For instance, GDLs are almost always rendered hydrophobic by application of a hydrophobic polymer coating, usually PTFE (poly-tetra-fluoro-ethylene) or FEP (fluorinated-ethylene-propylene). Another technique is the addition a so-called microporous layer between the GDL and the catalyst layer, though the actual function of this layer remains unclear. The microporous layer is not studied in this work. Though these techniques help to address this problem to some extent, liquid water continues to be a major engineering challenge for PEMFC leading up to its commercialization.

Innovative designs, modelling works and experimental diagnosis are being sought to investigate the phenomenon of water flooding inside PEMFCs. Effective flow field channels such as serpentine flow field [21], conventional flow field channels and inter digitated flow field

channels [17] are successfully employed in tackling water flooding issues. Modelling works which ranging from one dimensional, single phase and isothermal models [22, 23] to three dimensional, multiple phase and non-isothermal models[24, 25]have been purposed which highlight the issue of water management inside PEMFCs. There has been abundant research toward the development of experimental diagnosis tools that can investigate water flooding at different sections of PEMFCs. Some diagnosis tools are available for direct visualization [20, 26] and neutron imaging [27]for monitoring the dynamics and water distribution inside PEMFCs. Recently developed experimental tools which can measure the physical indicators such as pressure drop[28], local current density, local elevated temperatures and capillary pressure curves [1, 3] has been successfully employed as a diagnosis tools to measure the extent of water flooding and movement of water inside operating fuel cells.

Though these efforts have been very helpful to understand water movement inside PEMFCs, a much deeper understanding of water behavior, mass transfer properties and multiphase flow phenomena inside the gas diffusion layer is required at fuel cell operating conditions than currently exists.

2.5. Gas Diffusion Layer

The gas diffusion layer (GDL) is the electrode component of specific interest in this work. The GDL is required in the cell to compensate for the fact that the flow field geometry must be in a channel-rib arrangement. Without a GDL the areas under the rib are fully masked to oxygen, while areas over the channel have limited electron access. Because the GDL is positioned between the flow field and the catalyst layer it mediates virtually every transport process in the cell. As such it must serve numerous functions: 1) facilitate uniform reactant gas transport from flow field channels to catalyst layers, 2) provide electronic conduction from bipolar plates to catalyst layers, 3) conduct heat from membrane catalyst layer to coolant channel located in bipolar plates, and 4) provide mechanical strength to membrane in case of pressure differences between the anode and cathode gas. Figure 5 shows SEM image of a GDL electrode and highlights GDL functions and water transport behaviour inside PEMFCs. GDLs are almost

exclusively made from carbon-fiber paper. Graphitised carbon-fiber is an ideal material for GDLs because it is strong, light, has high electrical conductivity and because it is chemically inert and stable inside fuel cell. GDLs are typically between 150-400 µm thick with porosity between 70 – 90%. The fibers are about 10 microns in diameter and the pores range from 10 to 100 microns in diameter. An ideal GDL should possess hydrophobicity so that water does not wick and spread throughout the pore structure, high effective gas diffusivity which requires high porosity and low tortuosity, high permeability to support liquid water capillary flow. The proper characterization of GDL is critical for the optimization of PEMFC performance. A great deal of effort has been direct to this area in the past decade [29-34]. Studying the porous properties of the GDL is a challenge because most of the existing techniques used for conventional porous materials such as rock and sand are not suitable since GDLs display many atypical characteristics (they are thin, highly porous, compressible, electrically conductive, neutrally wettable, anisotropic, and so on). As such, experimental techniques must generally be developed that are adapted to the atypical features unique to the GDL.
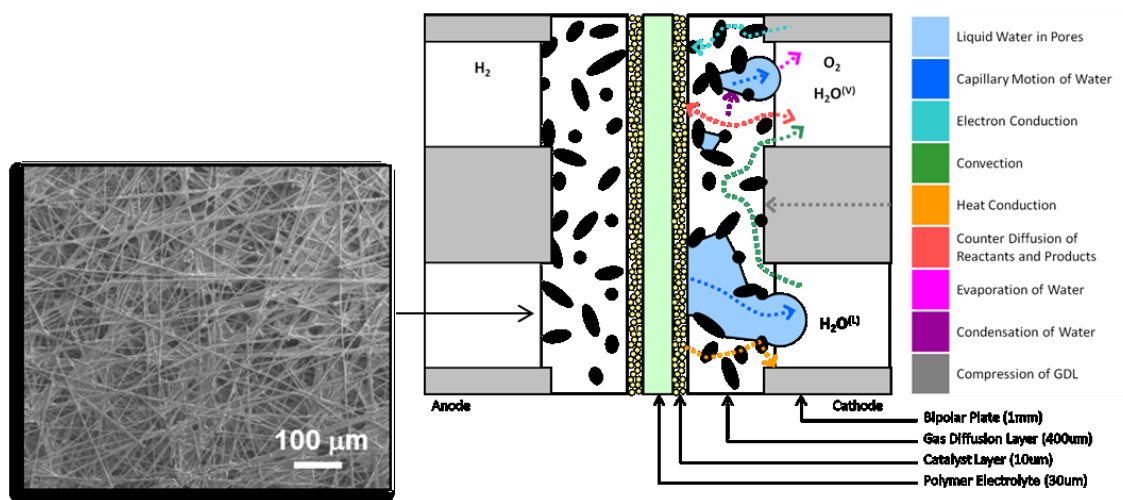
Figure 5: Schematic diagram highlighting role of GDL inside PEMFC and SEM image of GDL.

2.5.1. Hydrophobic Treatment of GDL

Because of its outstanding chemical resistance and non-wetting properties, PTFE coating has been widely applied to improve the water management function of the GDL in PEMFCs. SEM images of GDLs treated with PTFE are show in Figure 6below. PTFE treatment imparts

hydrophobicity to GDL surfaces with the intention of creating hydrophobic pores that remain open (in the presence of water) for gas transport between the flow channel and catalyst layer. It has been well documented that PTFE treatment in the GDL has improved cell performances by improving water and gas transport. In general, PTFE concentration in GDL varies from 0% to 40%. Various works relate to optimizing PTFE loadings in GDL for maximum water management have been reported [35]. Recent work by Chang et al[36], has indicated that the optimum PTFE on cathode GDL for maximizing the output power for PEM fuel cell is 5% without MPL with compression ratio of 30%, while with an MPL its 30% PTFE with compression ratio of 30%. Some studies have shown that maximum PTFE loadings in GDL can have a negative impact on water flooding[37].
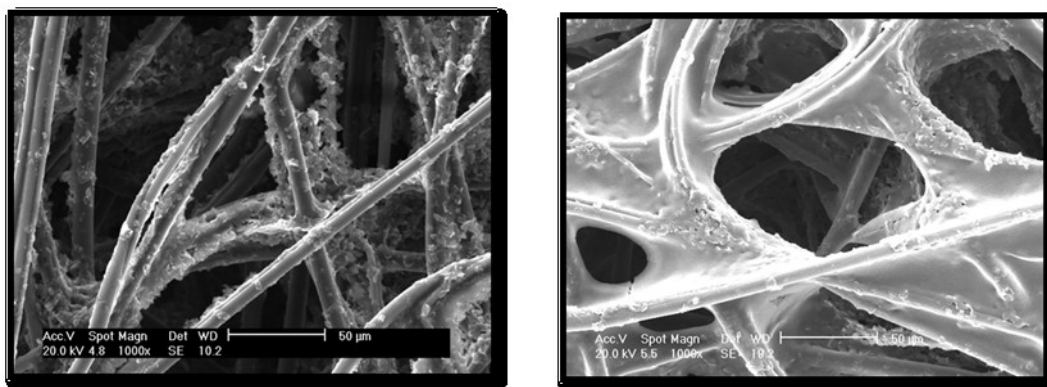
Figure 6: SEM images of GDLs treated with PTFE.

Clearly, there is still conflicting notions about the optimum hydrophobic treatment. This uncertainty has lead to the development of numerous wettability based characterization techniques. The wetting characteristic of GDL is manifested by its air-water capillary behaviour. Capillary pressure is the driving force for the water transportation and water distribution in GDL. Fairweather et al [3] were the first to report that GDLs displayed unusual capillary behavior with positive liquid pressure required to inject liquid water, yet negative pressure to remove it. This type of extreme hysteresis is not unheard of, but it is not common in most porous materials. It was unexpected to see this behavior in GDLs since they are considered to be hydrophobic once they have been treated with a PTFE coating. Shortly thereafter, Gostick et al[1] reported capillary properties of a range of GDL materials with varying PTFE loadings. They

reported that samples containing 10wt% and 20wt% PTFE displayed identical behavior, suggesting that typical commercially available PTFE coatings were not being applied effectively. Optimizing cell performance through altering the GDL thus requires a better understanding of the relationship between wettability and capillary properties of the GDL.

3. Theory

3.1. Wetting Phenomenon and Theory

Wetting is the tendency of one fluid to maintain contact with solid surfaces. This depends on the properties of solid and fluids (usually a liquid and a gas) that constitute the system. This is typically gauged by measuring the contact angle that a droplet of liquid forms on a flat substrate. Systems on which a liquid forms a spherical droplet are non-wetting, while systems where the fluid spreads into a film are called wetting. Because water is such a common liquid, the terms hydrophilic and hydrophobic are used to describe these two cases, respectively, when water is the liquid. Wettability plays an important role in the capillary behavior of porous solids. Porous solids are often modeled as bundles or networks of capillary tubes. When a single capillary tube is placed in a pool of fluid, the fluid will rise in the tube if the solid is wetting to the fluid and conversely it will depress if it is non-wetting. Hence, according to this picture pressure must be applied to inject a non-wetting fluid into a porous material and fluid will spontaneously imbibe into a wetting material. Measuring the pressures required to inject (withdraw) a fluid into (from) a porous material provides the capillary pressure curve and is an important characterization tool for porous materials.

Capillary pressure is the pressure difference across the interface of two immiscible fluids. It is usual to consider one phase as wetting and other non-wetting. The wetting and non-wetting phase can be either fluid depending on the wettability of the fluid with the solid surface. Consider the capillary rise of water in a glass tube, water is the wetting phase and the air is non-wetting, but replace water with mercury and the air will be wetting phase and the mercury will be non-wetting phase. In general, capillary pressure is defined as:

$$P_c = P_{Non\ Wetting} - P_{Wetting} \qquad \text{(6)}$$

The Young-Laplace equation gives a relation between capillary pressure, surface tension of the fluid and curvature of the interface between the phases as:

$$P_c = 2\sigma H \qquad \text{(7)}$$

Where σ is the surface tension of fluid and H is mean curvature of the interface. The mean curvature between two fluid interfaces having radii r_1 and r_2 is given by:

$$H = \frac{1}{2}\left[\frac{1}{r_1} + \frac{1}{r_2}\right]$$

(8)

In the case of cylindrical tube, the mean curvature of the interface can be found by geometric considerations from the radius of the tube and the contact angle formed the solid-liquid interface. Hence, Eq.(8)can be modified as:

$$P_c = \frac{-2\sigma_{LV}\cos\theta}{r}$$

(9)

Where r is the radius of the cylindrical tube and θ is contact angle measured through the fluid phase of the liquid droplet on the flat surface of solid. Eq. (8)is known as the Washburn Eq. and it is very widely used to interpret capillary pressure curves. Eq. (8) is not reliable for complex pores with realistic geometry [10], so interpreting capillary properties using Eq.(8)will be an approximation. This approximation is generally good for highly wetting or non-wetting systems, but fails for intermediate wettability systems such as the GDL. Due to its simplicity, however, the Washburn equation is ubiquitously used to relate pore size, surface tension, wettability and capillary pressure. The effect of temperature on capillary pressure can be obtained by simply taking the derivative of Eq.(8)with respect to temperature (T):

$$\frac{\partial P_c}{\partial T} = \frac{2}{r}\left[\frac{\partial \sigma_{LV}}{\partial T}\cos\theta + \frac{\partial \cos\theta}{\partial T}\sigma_{LV}\right]$$

(10)

Rearranging Eq.(10) yields:

$$\frac{1}{P_c}\frac{\partial P_c}{\partial T} = \frac{1}{\sigma_{LV}}\frac{\partial \sigma_{LV}}{\partial T} + \frac{1}{\cos\theta}\frac{\partial \cos\theta}{\partial T}$$

(11)

The first quantity on the right hand side of Eq.(11) accounts for the effect of temperature on the surface tension of liquid which is a decreasing function of temperature[38].The second quantity is the temperature sensitive contact angle. The temperature sensitivity of contact angles for many fluid-solid systems has been measured, and these will be discussed in Section 3.3 below.

She and Sleep[8] reported that the capillary pressure curve of porous substances shifted towards lower capillary pressure with increased temperature, and that the decrease is more

than can be explained by the decrease in the surface tension of water alone. This means the wettability of porous substances also changes with temperature owing to the second quantity in Eq.(11). Lim and Wang[11] measured contact angle directly on FEP coated GDL materials at different temperatures and reported that GDL wetting angle actually decreases with increase in temperatures. However, contact angle is a complex phenomena and translating capillary pressure curves on the bases of measure GDL wetting angle is not reliable for several reasons[39] which is described in detail below.

3.2. Temperature Dependence of Surface Tension

The surface tension of a liquid describes the ability of liquids to behave like a thin, elastic film. This property is mainly due to the intermolecular attraction between the liquid molecules at or the near surface with the rest of the fluid molecules. It is because of this property that liquids are able to hold some light objects on their surface. We know that the surface of any liquid is the interface between that liquid and another medium. For example the top surface of water in a container is an interface between the water and the air above it. There is also an interface between the water and the wall of the container. There is also an interfacial tension associated with this interface, as well as the gas-solid interface above the liquid. When two surfaces meet, they form a contact angle,θ, which is the angle between the surface and a line tangent to fluid at the point of solid-fluid contact, as shown in Figure 7. The equilibrium relationship between contact angle and interfacial tensions when a liquid drop rests on a solid surface is given by Young's equation:

$$\frac{\sigma_{SV} - \sigma_{SL}}{\sigma_{LV}} = \cos\theta \tag{12}$$
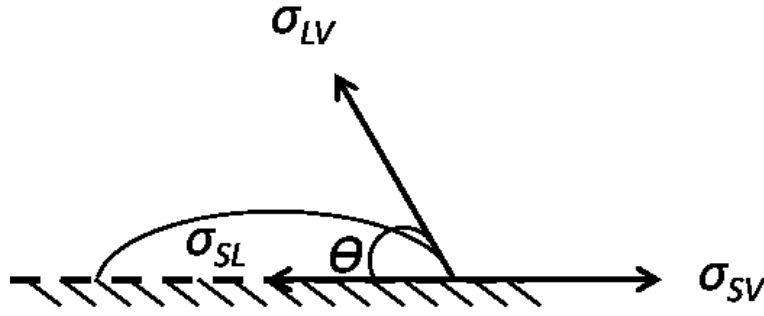
Figure 7: Contact angle and interfacial tension of a liquid drop on solid surface

Combining Eq.(8)and (12) gives:

$$P_c = \frac{2(\sigma_{SV} - \sigma_{SL})}{r}$$ **(13)**

Eq. (13) gives the mechanical and thermodynamic equilibrium of the concave interface of a liquid and its vapour in a pore with a mean radius r[40]. But for most systems, the interfacial tensions σ_{SV} and σ_{SL} cannot be measured accurately[41], thus for most liquid- solid capillary systems, Eq.(9) is usually used to interpret capillary pressure in terms of measurable quantities like liquid-vapour interfacial tension σ_{LV} and contact angle θ.

During the 1950s, Phillip and de Vries [42] had developed a model describing the simultaneous transfer of energy, liquid and water vapour in porous substances. They reported that the capillary properties in porous substances are only a function of temperature dependant surface tension in porous materials that are perfectly wetting such as water in acid washed quartz glass. In such a situation the contact angle is 0,$cos(\theta)$= 1 and Eq.(11) becomes:

$$\frac{1}{P_c}\frac{\partial P_c}{\partial T} = -\frac{1}{\gamma_{LV}}\frac{\partial \gamma_{LV}}{\partial T}$$ **(14)**

they reported that capillary pressure decreased with an increase in temperature in agreement with the fact that the interfacial surface tension of the fluid is a decreasing function of temperature [38].They had reported that the relative change in capillary pressure with temperature was equal to that of the temperature dependent surface tension of water. In reality the change of capillary pressure is roughly four times greater than relative change in

surface tension of water with temperature[43]. Further studies were undertaken by many geophysics and petroleum engineers both in laboratory and field studies [44-48]. Most of their results could not be explained by the change in air-water surface tension alone[49].These experiments were generally conducted in actual soil or core samples which contain many dissolved impurities. Since the leaching of these impurities can have a pronounced effect on the thermodynamic properties, including surface tension and contact angle, it is probable that the unexpectedly large effect of temperature on capillary pressure is due to the influence of these impurities. Interestingly, She and Sleep[8] reported air-water capillary pressure data for pure glass beads and sandstones, and found also disparity between the observed shift in capillary pressure and surface tension with temperature. Grant and Salehzadeh [40]included the temperature dependence of contact angle in their work formalizing the thermodynamic foundations of capillarity in porous materials. Therefore, it is imperative to consider the wetting angle and its temperature derivatives to scale precisely the effect of temperature upon capillary pressure in a porous material.

3.3. Temperature Dependence of Contact Angle

The wettability of a liquid on a solid surface is conveniently quantified by the contact angle formed between the liquid droplet and the solid surface as shown in Figure 7. A contact angle of 90° is almost universally used to distinguish between wetting and non-wetting. As shown in Figure 8, a contact angle below 90°C generally indicates that the liquid is wetting and a contact angle above 90° means non-wetting. This definition stems directly from the Washburn Equation (Eq.(8))) where the $\cos\theta$ term changes sign at $\theta = 90°$ which corresponds to a change in the sign of capillary pressure and hence wettability. This leads to the prediction that a liquid with a 89° contact angle will spontaneously imbibe while a liquid with a 91° contact angle must be forced into the porous material. Real porous materials (with non-cylindrical pores) do not behave in this way of course, but the use of 90°as the transition point persists.

Non –wetting   Wetting
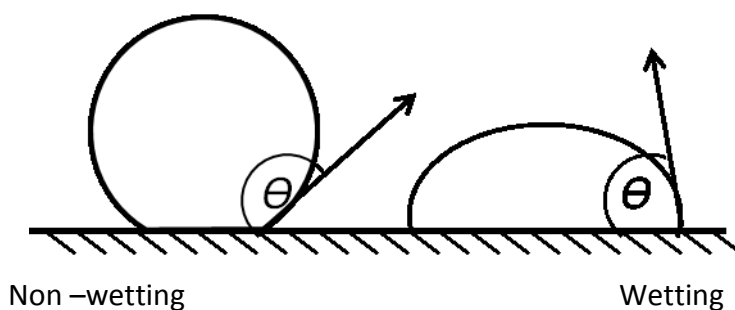
Figure 8: Wetting and non- wetting according to contact angle.

In his review papers on wettability in porous materials Anderson[50] has proposed that true hydrophilic behavior (spontaneous imbibition of liquid water) occurs when the contact angle is in between 0 and 60-75°, and true hydrophobic behavior (spontaneous eject of liquid)can only be expected when the contact angle is above120-135°. When the contact angle lies in between them (contact angle near 90±30°) then the solid is considered to be neutrally wetting.   Despite the fact that contact angles do not precisely define the boundary between wetting and non-wetting, they do still influence the capillary pressure and fluid behavior.

Contact angles have an important role in a number of technological, environmental and biological phenomena and processes. They are also the manifestation of wettability and surface tension of solid. The contact angle measurement is the simplest way to interpret solid surface tension[39]. Unfortunately, in spite of this simplicity, contact angles are a complex phenomena[51]. For instance, the contact angle made by an advancing liquid and that made by a receding liquid are not identical as shown in Figure 9. Almost all the solid surfaces exhibits contact angle hysteresis. Contact angle hysteresis may be due to roughness and heterogeneity of the surface[52].
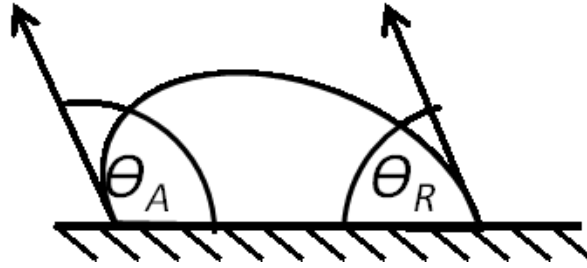
Figure 9: Contact angle hysteresis; θA andθR are the advancing and receding contact angles formed when a droplet moves towards left.

If roughness is the primary reason, then the measured contact angles are meaningless in terms of Young's Equation (Eq.(12)) because it was derived on the basis of smooth, homogeneous, isotropic and non-deformable solid surfaces. On very rough surfaces, contact angles are larger than chemically identical, smooth surfaces due to the increased contact angle between the solid and liquid for a given projected area created by the surface as shown in Figure 10. The thermodynamic equilibrium angles on rough and heterogeneous surfaces are called Wenzel [52]and Casie-Baxer angles[53] respectively.

Wenzel State   Cassie-Baxter State   C-B-W State
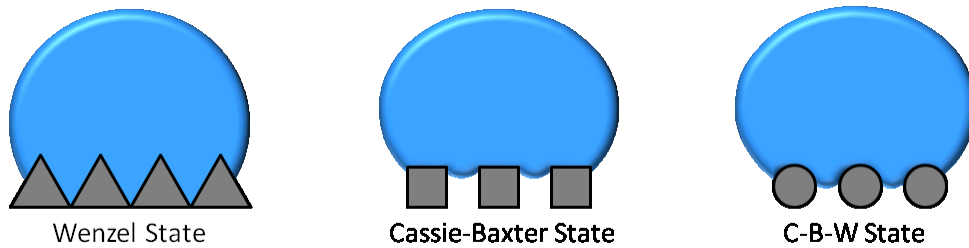
Figure 10: Droplet on rough surfaces.

The GDL wettability is the result of chemical heterogeneity (graphite and PTFE), surface roughness and the complex pore structure of GDL materials. The fibres of GDL materials are made of graphite, which has a water contact angle of 86°[54] and therefore should be expected to exhibit neutral wetting. Although raw graphite GDLs are known to display some hydrophobic tendencies[2], it is still desirable to render them as hydrophobic as possible. Any hydrophilic behavior is not advantageous for fuel cell operation, as water tends to spread throughout the GDL pore network and block gas transport to the catalyst layer. PTFE is reported to have water

a contact angle of 108°[55]. As water contact angles of both graphite and PTFE fall in the region of neutral wettability, it is not expected that GDL will display extreme water repellency. In fact, GDL surfaces contain a mixture both PTFE (slightly hydrophobic) and pure graphite (slightly hydrophilic) regions. Sinha et al[56] attempted to incorporate this dual nature into a pore network model but they used the Washburn Eq. to relate size to pressure so wettability changes were solely due to the changing sign of the $\cos(\theta)$ term. The presence of hydrophilic pores in GDL materials is supported by some of the experimental results by Gostick et al[57] which shows negative capillary pressure is required during the withdrawal of water from the GDL pores.

The importance of the temperature on contact angle has been well studied [54, 58-60]. As can be seen in Figure 11, the temperature dependent contact angle of water behaves differently on various solid substrates. The contact angle for water on a copper substrate is shown in Figure 11as an example of the extreme behavior that might possible occur. As can be seen, the angle remains somewhat constant for a temperature range of 60°C and then it increases drastically with increasing temperatures. The contact angle of water on PTFE, FEP and graphite surfaces of relevance to fuel cell electrodes are also shown. The contact angle of water on PTFE surface remains constant with increasing temperature up to 100°C, while FEP (another fluoropolymer) shows a trend of deceasing contact angle with increasing temperature. The contact angle on graphite increases somewhat, at a reported rate of +0.06 °/°C[61]. Despite having these temperature dependent contact angles it is not feasible to predict shifts in capillary pressure based on them. These values only suggest that any changes in capillary behavior will be moderate, and perhaps in which direction.
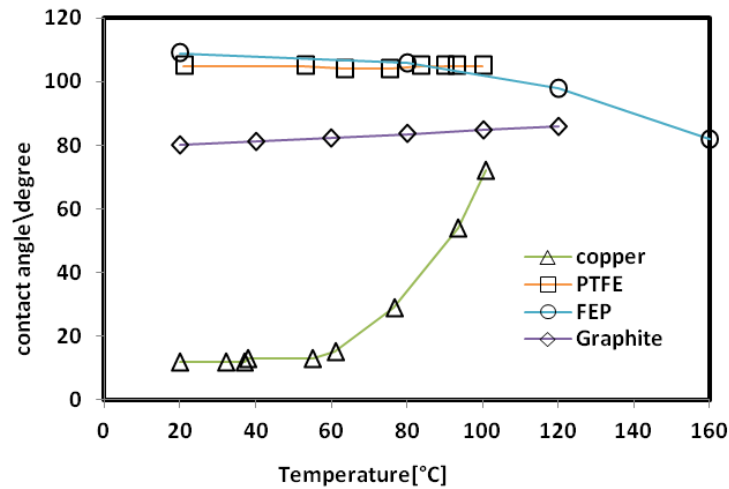
Figure 11: Temperature dependent contact angle of water in various surfaces[59].

3.4. Capillary Pressure Curves

A capillary pressure curve provides essential information about a porous system such as porosity, breakthrough pressure, fluid–solid wettability, and pore size distributions. A porous medium can be envisioned as a network of connected pores of different sizes, and thus a range of capillary pressure is required to invade all of these pores. According to the Washburn equation (Eq.(1)), the larger pores will invade first and smaller pores last. A capillary pressure curve is obtained by gradually draining a wetting phase from the porous medium by increasing the pressure of the non-wetting phase and monitoring non-wetting phase saturations at each pressure step. The capillary pressure and saturation relationship (or curve) depends on the interaction of wettability, pore structure, initial saturation and saturation history[50].

One important feature of capillary pressure curves is they are influenced by both the solid geometry and the fluid-solid wettability. Mercury is often used as the invading fluid since it highly non-wetting on virtually every surface, and as such differences in mercury intrusion data between samples can be entirely attributed to pore size. Capillary pressure curves are also influenced by wettability as well, so using water as the invading fluid on two samples with identical pore structure will reveal differences in wettability. In the present work it is the latter information that is sought, so water is used exclusively. A typical capillary pressure curve of air-water system for GDL electrodes is show in Figure 12. Different parts of a capillary pressure

24

curves are described in Section 3.4.1. The general method employed to measure capillary pressure curves is described in detail in Section 3.4.2.

3.4.1. Drainage and Imbibition Capillary Pressure Curves

Drainage is the process of displacing a wetting phase by a non-wetting phase while reverse is term imbibition. A typical capillary pressure curve for GDL air-water system is shown in Figure 12. The experiment is started at highly negative capillary pressure during the drainage process. Accordingly, the volume of non-wetting fluid injected into the sample is zero and the volume of the wetting fluid in the sample is maximum. As described earlier, a positive capillary pressure is required for non-wetting phase to invade into GDL pores. So, positive capillary pressure is categorically increased by reducing gas pressure that allow non-wetting phase to invade GDL pores increasing its saturation. Accordingly, the drainage capillary pressure curve is obtained by reducing the wetting phase saturation from its maximum to the irreducible minimum which is achieved by increasing the capillary pressure from zero to a large positive value. Conversely, the wetting phase saturation increased to obtain the imbibition curves. The imbibition curves can be further distinguished as spontaneous imbibition curve and force imbibition curves. The spontaneous imbibition curve is determined immediately after the drainage capillary curve. The capillary pressure is decreased to zero, allowing the wetting phase to imbibe. As shown in Figure 12, the GDL system does not exhibit any spontaneous imbibition. The second portion is the forced imbibition curve, where the capillary pressure is decreased from zero to a large negative value. There exists only forced imbibition curves and the forced imbibition ends with the residual non-wetting phase.
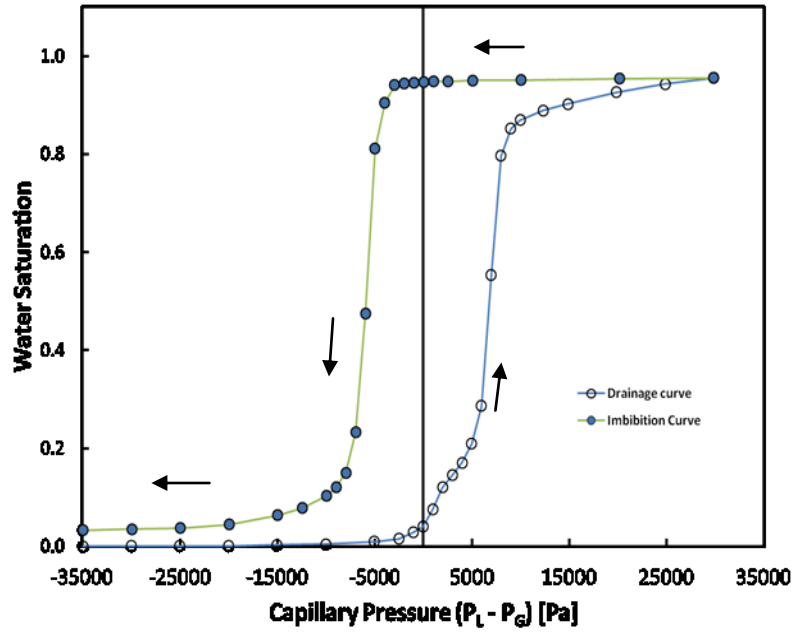
Figure 12: Capillary pressure and saturation relationship for GDL air water system showing drainage and imbibition curves: hollow circles represent drainage and solid circles represent imbibition.

As can be seen in Figure 12 capillary hysteresis is always present, which is the difference between the injection and withdrawal curves. There are several reasons for the capillary pressure hysteresis. Contact-angle hysteresis is one cause as shown in Figure 9. During drainage, the non-wetting phase displace the wetting phase, so the contact angle between the fluids will be the receding angle ,Θ_R, During imbibition the advancing contact angle ,Θ_A, is formed between the fluids, when the wetting phase saturation increases and displaces non-wetting phase from the pores. Also, drainage is controlled by throat sizes, while imbibition is controlled by body sizes, so the mechanism of displacement and fluid pathway varies. Finally, the pore geometry can have a large impact on the operating interfacial curvature. For a given contact angle, the curvature can be positive or negative depending on if the pore walls are diverging or converging. Given the fibrous nature of the GDL solid structure, there are clearly many diverging-converging throats.

3.4.2. Method of Measuring Capillary Pressure Curves

Mercury Intrusion Porosimetry(MIP) is one of the widely utilised methodologies to measure capillary pressure curves in porous materials. However, as mentioned above this method is not

suitable to measure wettability, as mercury is highly non-wetting to all materials. To obtain meaningful data on the behavior of water in the GDL it is necessary to use water. Water is widely used as a working fluid in many fields such as hydrology, but GDLs present several unique challenges. They are very thin and compressible, low pore volume, finite size (meaning that surface effects GDLs are real and important), most critically, the wettability is essential, so a method for injecting and removing water was needed. A number of methods have been developed in the past few years which are discussed in a book chapter by Gostick et al[2]. The two main methods are highlighted below:

a) Volume Controlled Porosimetry

In this approach, water is injected into the sample directly with a syringe pump. Fairweather et al[3] used a syringe pump to inject discrete amounts of water into the GDL sample while measuring liquid pressure at each step. They were able to scan the water saturation in both the increasing and decreasing capillary pressure directions and were the first to report the large hysteresis that spans the P_C = 0 axis. Harkness et al [5]also used a syringe pump and a similar sample holder as to Fairweather et al, but, they used continuous injection. As discussed by Gostick et al, the Harkness approach is a viable technique, but it was not considered in the present work since the ability of a syringe pump to operate reliably in a 90°C oven was a concern.

b) Pressure Controlled Porosimetry

Gostick et al [1, 62] proposed a method by which the capillary pressure in the GDL sample is varied directly by controlling the gas pressure above the sample. The water volume in the sample was tracked by measuring the amount of water uptake from a water reservoir on an analytical balance. This method can scan the capillary pressure curves for the GDL sample over a wide range of positive and negative capillary pressures. As this approach employed an analytical balance to monitor water volume, and this is also unlikely to function well in a 90°C oven. An alternative approach was identified for measuring water volume, as described in the next section.

4. Experimental

4.1. Overview of Experimental Setup

The schematic diagram of experimental setup is shown in Figure 13. A brief overview is given here, and each component is described in more detail in the following sections. In order to provide elevated temperatures the entire setup was placed inside and oven (Yamato model DKN402/602/812/912). The special feature of this device is that rather than utilising the delicate analytical balance to measure water uptake to the GDL sample as in previous methods[1], it utilizes a temperature compensated and highly accurate differential pressure sensor (Omega-MMDWU10WV10K2B0T2A2S) to measure the height of a water in a tube of known diameter to track water uptake and withdrawal in the GDL sample. The capillary pressure in the sample is increased or decreased by controlling the gas pressure above the sample with the help of a syringe pump placed outside the oven and connected via a tube through an access port. The movement of the syringe pump (Harvard 11-Plus) is controlled by LabView through an RS-232 interface. An absolute pressure gauge (Omega PX409-030A5V) is used to measure the gas pressure (P_G) and a barometer (Omega PX2670-600A5V) provides the atmospheric pressure (P_{ATM}).Thermocouples are installed at two locations as shown in Figure 13 to measure the temperatures of water near the sample and inside the oven. A photo of the experimental setup is shown in Figure 14. Photos of these instruments are shown in Appendix B.

One unforeseen problem was caused by the significant thermal expansion of water in the piping during heating and cooling stages. It was necessary to add a water reservoir to help act as a surge tank to regulate the height of the water inside the capillary tube during periods of temperature changes. The water reservoir is coupled to a solenoid valve, which can be opened by computer during heating and cooling stages, then closed during measurements.
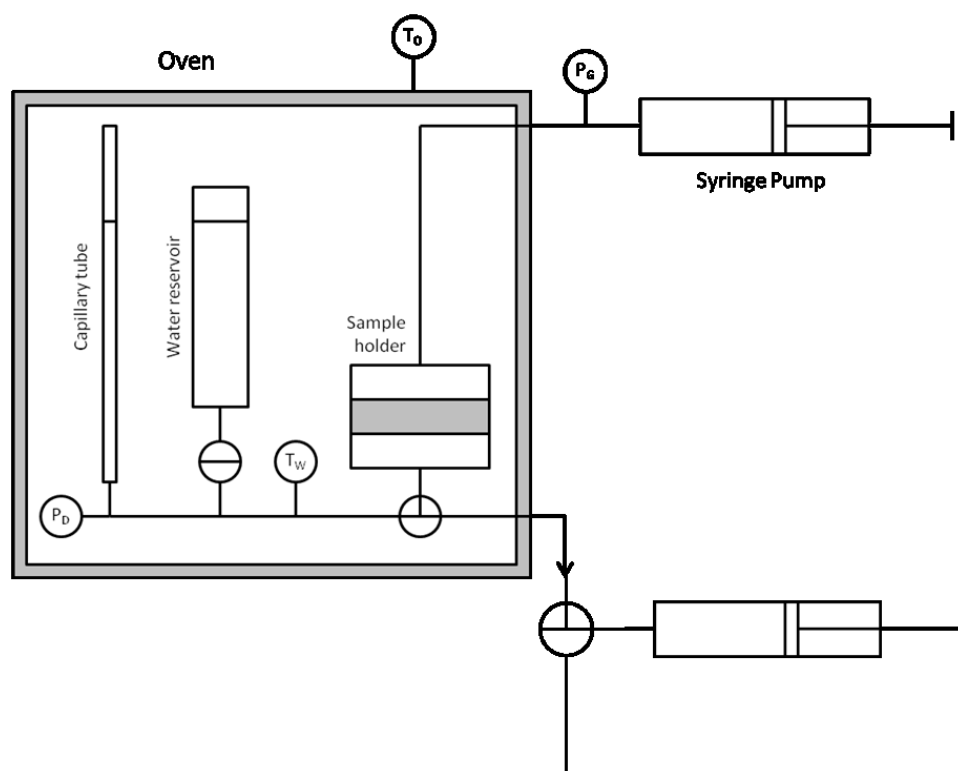
Figure 13: Schematic diagram of experimental setup.
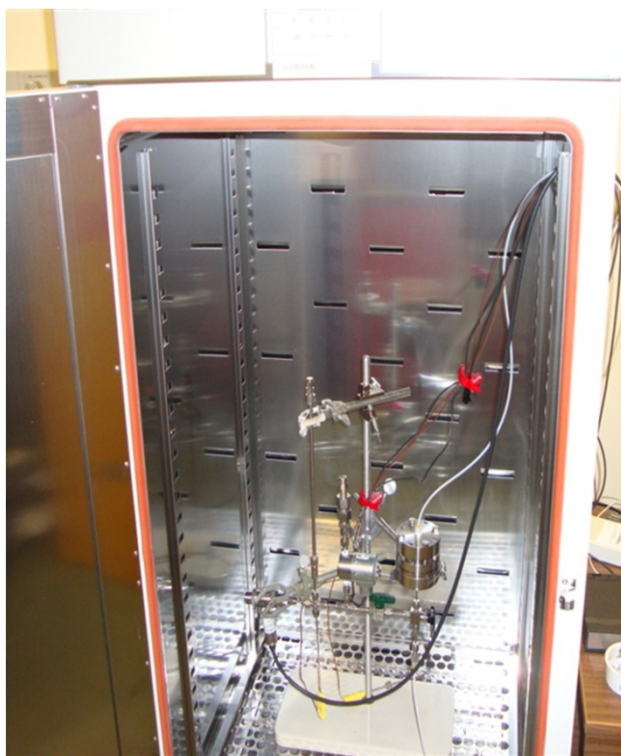
Figure 14: Photo of the experimental setup.

4.2. Sample holder

The schematic diagram of the sample holder is shown in Figure 15. Detailed instructions for assembling the various components are given in Section4.5 below. This holder was first described by Gostick et al [62] and was used here with no changes. The base plate consists of a liquid port and it holds the liquid distributor which distributes the liquid uniformly in the GDL sample. A hydrophilic membrane (Millipore, 0.2μm PVDF # GVWP0700) is placed below the GDL sample and acts as a capillary barrier. This membrane allows water to flow into the sample through but stops air from entering the water piping. The middle plate is designed to hold a GDL sample of 0.01905m diameter. The sample is located above the hydrophilic membrane with the help of a sample locating gasket. A specially-designed compressing cylinder holds the GDL sample tightly with the help of a plug and set screws. A hydrophobic membrane (Satorius, 0.45μmPTFE# 11806-25) above the sample allows air to pass through but stops water as it breaches the GDL. The top plate consists of a gas port through which gas pressure sample is controlled above GDL sample. The top plate is bolted to the bottom plate through holes on the middle plate. This allows the top plate to push down on the compressing cylinder and create a liquid tight seal between the hydrophobic membrane and the PTFE locating gasket. The plug moves inside the compressing cylinder and pushes down on the hydrophobic membrane and sample. Applying 'finger tight' tension to the setscrew is sufficient to prevent the hydrophobic membrane from bulging at high positive capillary pressures. Additional force on the set screw will result in GDL compression as explored by Gostick et al. [1].Technical drawings of the sample holder provided in Appendix C.
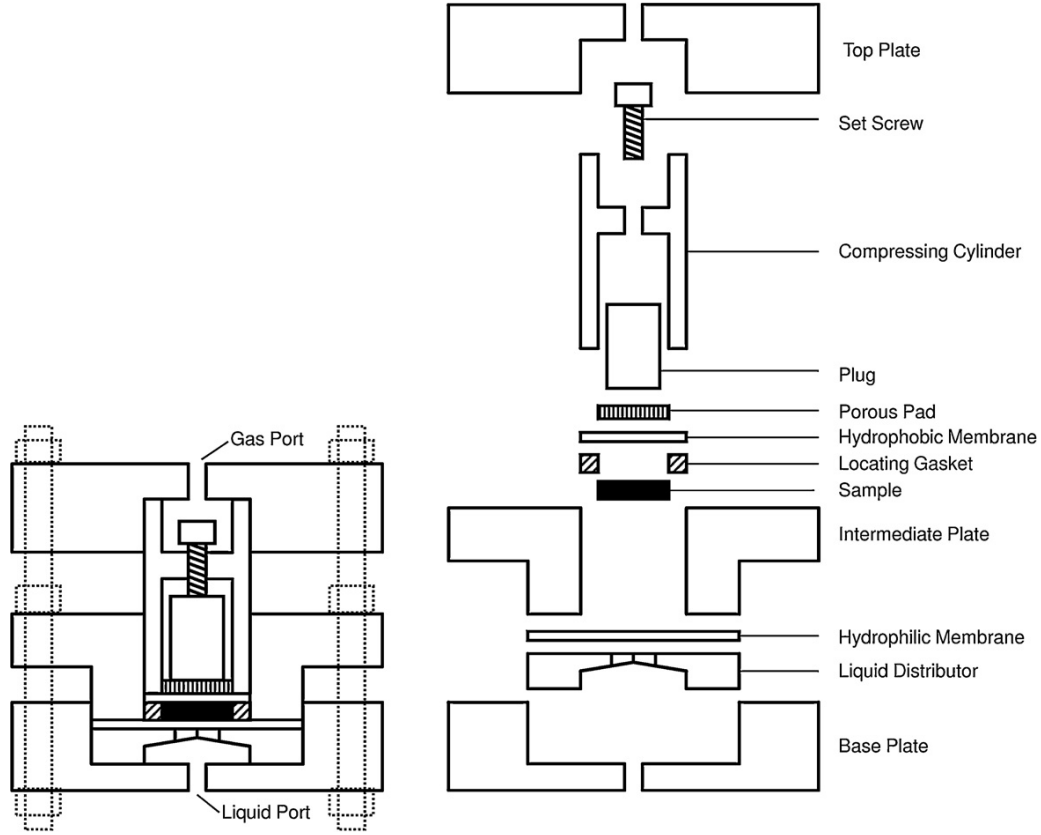
Figure 15: Expanded view of sample holder[1].

4.3. Water Uptake Tracking

One of the main challenges in developing this experimental setup was the tracking of water uptake and withdrawal in the GDL sample. This was accomplished by monitoring the change in height of water in a vertical capillary tube connected to the liquid side, as shown in Figure 13. The chosen capillary was a stainless steel 304 tube with an internal diameter of 0.9266 mm. The differential pressure sensor was specifically chosen for its very high accuracy of +/- 0.05% and reported thermal stability up to a temperature of 93°C within an accuracy of 0.30%. As water moves in and out of the sample the height of water in the column changes resulting in a change in the measured differential pressure. As the gas side of the differential pressure sensor and the top side of capillary tube are opened to atmosphere, the differential pressure due to the water column of height h inside the capillary tube is given by,

$$P_D = P_L - P_G = P_{Atm} + \rho g h - P_{Atm} = \rho g h \tag{15}$$

where ,ρ is density of water, that is taken as a function of temperature, g is acceleration due to gravity and P_{ATM} is atmospheric pressure. Thus, pressure measured by the differential pressure sensor is equal to the head pressure of the water inside the capillary tube. The total liquid pressure exerted at the bottom of the GDL sample is equal to the measured liquid pressure minus the height difference between the sample and the sensor, which was fixed at about 8 cm below the sample. Converting this pressure reading to water volume is possible if the internal diameter of the capillary tube is known:

$$V = \frac{\pi}{4}d^2 \cdot h$$

(16)

Where V is volume of water and d is internal diameter of tube. The amount of water in the GDL at any point is equal to the amount missing from the tube. The diameter of the tube is found by calibration.

4.4. System Calibration

Calibrating the internal diameter of capillary tube used to measure volume is imperative to accurately calculate the volume of water using Eq.(16).To accomplish this, a micro-liter(Hamilton Gas tight, 250 μL) syringe connected the drain port of the system as shown in Figure 13.Water was injected into the system in 10 μL steps and the resulting increase in measured pressure head was monitored. Repeated injections and withdrawals were performed and no hysteresis was observed in the stainless steel tube. Glass tubes were initially used, but meniscus and hysteresis effects caused significant errors that were absent in the steel tube. The resulting pressure vs. water volume calibration curve was almost perfectly linear as shown in Figure 16, indicating no blemishes, bends or constrictions in the tube. Importantly, the straight line indicates that deflection of the pressure sensor membrane was not significant. This was a concern because the movement of the sensing membrane would result in significant changes in water level in the tube. The accuracy of the pressure sensor (0.05% FS or 3 Pa) means that the diameter of the tube can be estimated from the data in Figure 16 by inverting Eq.(16)to solve for d. The differential pressures data are utilized to calculate the corresponding heights of the water column inside the tube from Eq.(15).The data are utilized to calculate corresponding volumes of water using Eq.(16). The diameter of the tube thus obtained is

0.9622 mm, which was confirmed by physically measuring the internal diameter using a wire feeler gauge. The thermal expansion of the stainless steel tube at higher temperature was investigated and found to be negligible.
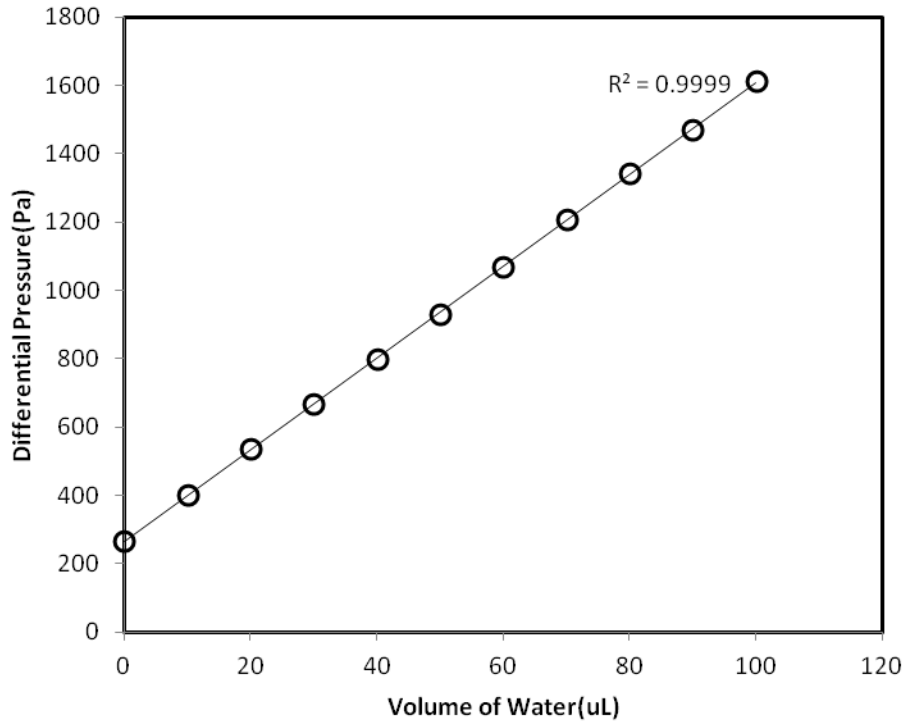
Figure 16: Calibration curve for internal diameter of capillary tube.

Water density is a function of temperature and so the temperature dependent density value is utilised to calculate the mass of the water. The 5th order polynomial fitting Eq.is given by Eq.(17)was used to relate relating density with temperature given by Eq.(17).The data fit very closely as shown on Figure 17.

$$\rho_{water} = 999.83974 + 0.0734107 \cdot T - 0.00878 \cdot T^2 + 7.07 \cdot \times 10^{-5} \cdot T^3 - 4.43 \times 10^{-7} \cdot T^4 + 1.229 \times 10^{-9} \cdot T^5 \quad \textbf{(17)}$$

Where ρ_{water} is the density of water in kg/m^3 and T is the temperature of water in degree Celsius. Eq. (17)is incorporated into Labview to calculate volume as a function of real-time temperature. The water temperature in the system was recorded continuously, so every calculation of water volume used a temperature corrected density value.
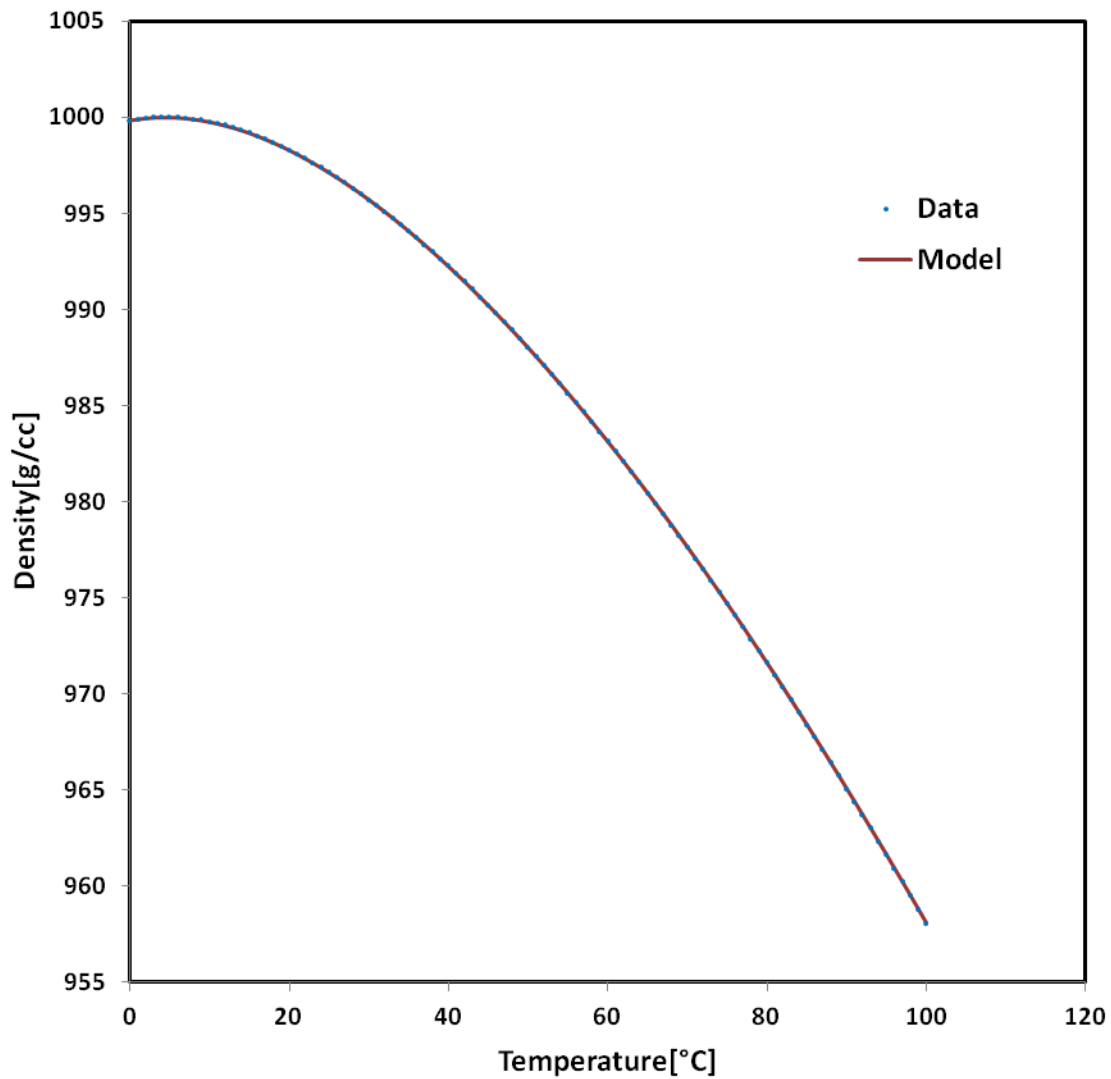
Figure 17: Experimental data for water density at different temperatures[63] (circles) and the polynomial fit through the data (line).

4.5. System Setup

There are two main steps to setting up a run. First all the piping must be primed with water. Then the sample holder is assembled. These steps are described below.

4.5.1. System Priming

It is important to carefully prime the system with water to ensure no bubbles are present. Bubbles dissolve into the water and compress under changing pressure, both of which impact the accuracy and reliability of the water volume measurement, and they hinder the flow of

water. Priming is best accomplished by filling each individual piece of piping and fitting with water as the system is assembled. It is recommended to use a syringe and needle to inject water into each part while allowing air bubbles to escape. The first step is to fill the piping below the sample holder (shown on the left hand side of the 3-way valve in Figure 13).Start by filling the cavity of the differential pressure sensor, then the vertical capillary tube and connecting piping. Once all the piping is filled and the water level in the system can be altered via a syringe connected to the drain port of the 3-way valve as shown in Figure 13.

The sample holder is primed by switching the 3-way valve and injecting water into the system via a syringe connected to the drain port. This water will fill the cavity of the bottom plate. Next the liquid distributor is dropped into the cavity of the bottom plate. As this plate is submerged liquid water will spout from the holes, and this should be free of bubbles. Next, a pre-saturated hydrophilic membrane is laid on top of the distributor followed by an o-ring. The next step is rather delicate. In order to hold the hydrophilic membrane in place during the addition of the middle plate it is best to apply some suction to the drain port on the 3-way valve. Hanging an open tube from the drain port of the 3-way valve usually suffices, but the middle plate must be installed quickly before the water drains from the bottom plate. The small pores in the hydrophilic membrane mean that flow is fairly slow, but speed is of the essence. Once the middle plate is installed, it is wise to check for bubbles under the hydrophilic membrane. Assuming there are none, then the priming of the system is completed by simply leaving the drain pipe hanging and waiting for the water to drain from the cavity of the middle plate, through the hydrophilic membrane. Once the water level reaches the hydrophilic membrane then flow will cease since the ~1m or -10,000 Pa of suction applied by the hanging drainage pipe is not sufficient to breach the 200 nm pores. Note that this initial suction is integral to not just the assembly and priming process, but also the sample mounting since it ensures that a negative capillary pressure exists in the system while the sample is mounted.

4.5.2. Sample Mounting

Once all the loose water has drained from above the hydrophilic membrane, a PTFE gasket of 1" OD and ¾" ID is placed into this hole. The thickness of the PTFE should match the thickness of

the sample to be tested. Next, a dry GDL sample with a diameter of 3/4" is placed into the hole of the gasket. A hydrophobic membrane with a 1" OD is loaded on top of the sample, which is followed by compressing cylinder with plug and set screw. The cylinder pinches the hydrophobic membrane to the PTFE gasket and creates a water tight seal. The plug prevents bulging of the hydrophobic membrane at high capillary pressures, as this would appear as GDL sample volume in the measurement. The top plate is bolted to the bottom plate (through holes in the middle plate) to seal the assembly. Finally, an allen key is inserted into the gas port on the top plate to tighten the set screw in the compression cylinder slightly without applying GDL compression.

4.5.3. System Start-up

After mounting the GDL sample, the gas port of the top plate is connected with the syringe pump. Next, a positive gas pressure of around 15kPais applied by manually moving the syringe pump. This pressure, along with the suction capillary pressure of -10kPa, creates a capillary pressure of -25kPaon the sample. This large negative capillary pressure assures that GDL sample is completely dry before starting the experiments and no water will spontaneously imbibe into the sample before the beginning of the experiment. Now, the 3-way valve is turned to connect the sample with water volume measurement system. The positive head pressure resulting from the water column inside capillary tube is very small and does not impact the negative capillary pressure applied on the sample. Next, the oven is turned on and the desired experimental temperature is set. Thermocouples are installed to measure the temperatures of the water inside the capillary tube and inside the oven as shown in Figure 13. As the temperature of the system gradually rises, water expands and rises inside the capillary tube. The overflowing water spills down from the top of the tube and evaporates. Since the system is very sensitive to temperature, it was essential to ensure that thermal equilibrium had been established throughout the system before taking any measurements. The temperature of water becomes equal to oven temperature thermal equilibrium is reached, but an additional few hours are given to be safe. This heating (or cooling) process usually takes12 hours. Prior to starting the experiment it is essential lower the water level in the system to some location below the tip of the vertical capillary. The solenoid valve at the bottom of water column is

opened for just a few seconds and water will flow from the capillary to the reservoir, or vice-versa to ensure that that the starting level of the water is at a suitable location (not too close to the top or bottom of the capillary).

4.6. Experimental Procedure

Following system setup, the syringe pump is started and its direction is controlled by Labview programming through an RS-232 interface. The pump compresses and expands the air above the sample as it moves forward and backward, thereby changing the capillary pressure on the GDL sample. The capillary pressure on the sample is given by,

$$P_C = P_L - P_G = P_{ATM} + \rho g(h - h') - P_G \qquad (18)$$

Where P_L and P_G are liquid and gas pressure on GDL sample, h is the height of the liquid in the capillary tube and h' is the height of the sample surface from the bottom of the liquid level in the capillary tube.

Desired capillary pressure points are fed to Labview through a pressure points input file such that the test starts at a high negative pressure until it reaches high positive pressures and returns to high negative pressure, completing one cycle. At each pressure point, the mass of the water in the capillary tube is monitored. The system is held at constant capillary pressure until mass of the water in the capillary tube becomes stable before it moves to the next pressure steps. Although liquid pressure does vary during transient water uptake due to viscous effect, it return to an original value, P_L, once the flow ceases. The transient responses of water uptake to changes in capillary pressure are indeed stable before each subsequent change in capillary pressure as shown in Figure 18. The cycle is repeated several times for primary and secondary water imbitions and drainages at desired temperatures. A single test at a given temperature requires at least 6 hours measuring two full loops.
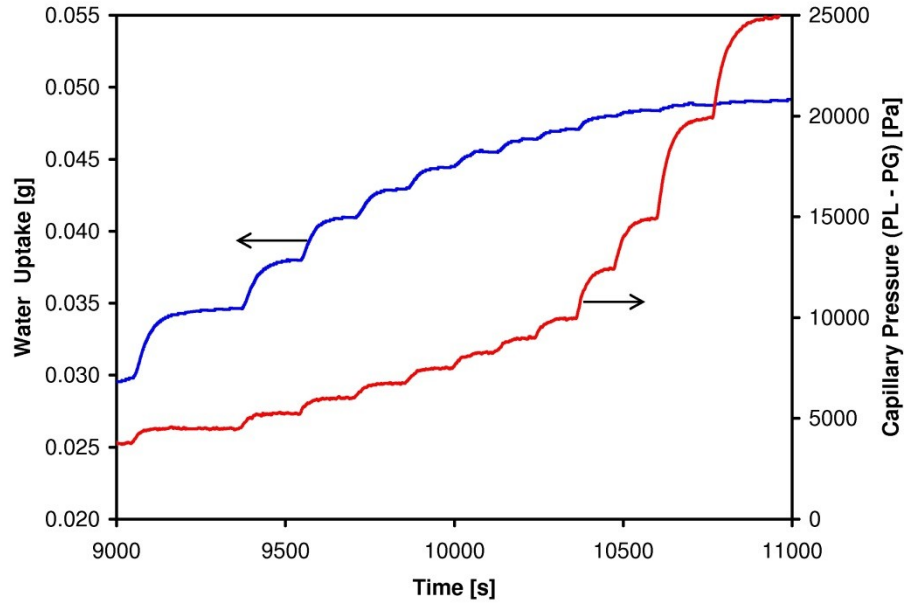
Figure 18 : Sample of raw data showing transient water uptake into sample as the capillary pressure is increased stepwise.

4.6.1. Sample Saturation Calculation

Since the sample is completely dry initially, water uptake by the sample equals amount of the water loss from capillary tube. The water saturation in the sample is computed by:

$$S_W = \frac{V_W}{V_P} = \frac{m_{W.}\rho^{-1}}{\frac{\Pi}{4} \cdot d^2 \cdot \delta \cdot \varepsilon} \tag{19}$$

Where V_W is the volume of water uptake in GDL sample, V_P is volume of GDL pores, m_w is mass of water in GDL sample, d is diameter of the sample, ρ is density of water which is taken as function of temperature as described in Section4.4. δ is sample thickness which is measured manually before testing with a help of a caliper. The evaporation loss of water from the system during the course of experiment (approximately 6 hrs) is minimised by using a stainless steel jacket outside of the capillary tube and also maintaining the gas above the sample fully humidified. However, small correction of evaporation loss of water is still done by calculating it as a product of rate of evaporation and time required to reach an equilibrium pressure at each pressure step. The evaporation rate is found by trial and error using a spreadsheet such that primary curves meet with secondary curves exactly at same point at highest saturation.

Evaporation loss thus calculated is subtracted to mass of the water in the GDL at each pressure point. The validity of this approach was investigated thoroughly by Gostick et al [62].

4.7. Temperature Protocol

The temperature protocol that was utilised to study the effect of increasing and decreasing temperatures on capillary pressure curves are shown in Figure 19. The sample is first tested at room temperature (20°C) and then the temperatures are increased step by step to run tests at 50°C, 70°C and 85°C respectively. Then, in some cases tests are run at decreasing temperatures down to 20°C at room temperatures. It takes about a week to complete the cycle of increasing and decreasing temperatures as shown in Figure 19 with each test requiring 12 hours to reach thermal stability and another 6 - 12 hours to run the test itself.
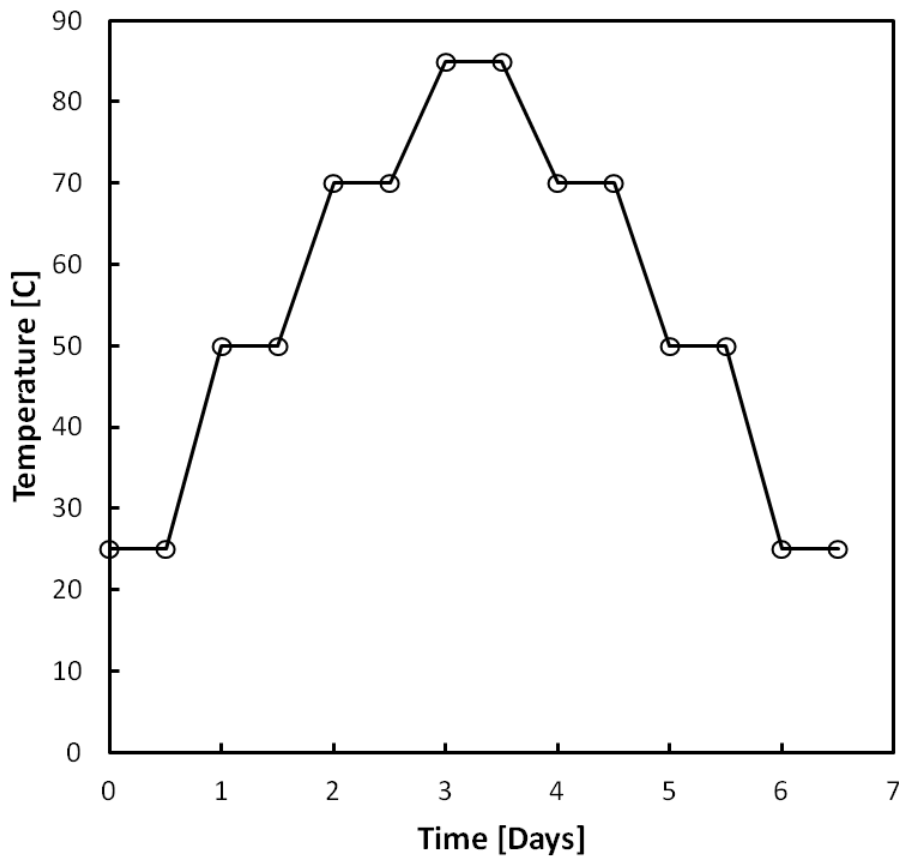
Figure 19:Experimental temperature protocols.

4.8. Method Validation

4.8.1. Comparison with Established Method

The new experimental setup developed here is very similar in most respects to the established method of Gostick et al. [1, 62]. To confirm that the present device was operating as expected, experiments were performed at room temperature utilizing a balance to measure water uptake (the original method) and compared to tests using a differential pressure sensor. Capillary pressure curves obtained by two methods are compared below. The tests performed with the balance are referred to as GCP.
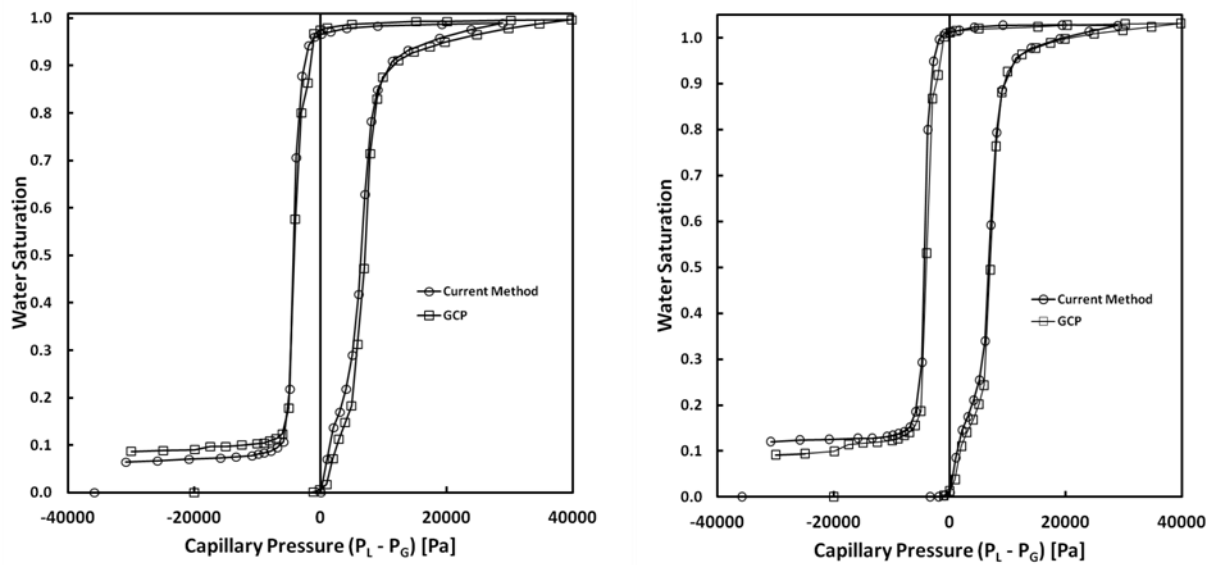
Figure 20: Pc-Sw curves for Toray090 using current method (Circles) and using GCP (Squares): Toray090 untreated (Left) and Toray090 5% PTFE (Right).

P_C - S_W curves for Toray090 with no hydrophobic treatment at room temperatures by the original and current method are shown Figure 20 (left) with the secondary curves omitted for clarity. As seen, capillary pressure curve obtained from two methods is almost overlapping during water injection and withdrawal. The slight differences at on the initial rise portion of the curves are likely due to differences in the samples. Both curves attained nearly full saturation at pressure about P_C =+10,000 Pa and water withdrawal starts at negative capillary pressure about P_C = -2,000Pa. The curves attained residual water saturation of at 0.01.Figure 20 (right) shows curves for Toray 090 with 5% by wt. PTFE added as a hydrophobic agent. Again both curves overlap very well with a small discrepancy during the withdrawal portion that is consistent

within the amount of variability generally seen between samples. Figure 21 compares the curves obtained with the original and current method for Toray090 with 10% PTFE (left) and 20% PTFE (right). As can be observed, both curves are almost overlapping during water injection and withdrawal. The close match between data obtained using the new method and the established and proven original device indicate that the vertical capillary tube approach to measure water volume is suitably accurate and not subject to any odd behavior, such as the bowing of the pressure sensor membrane causing unaccountable water loss.
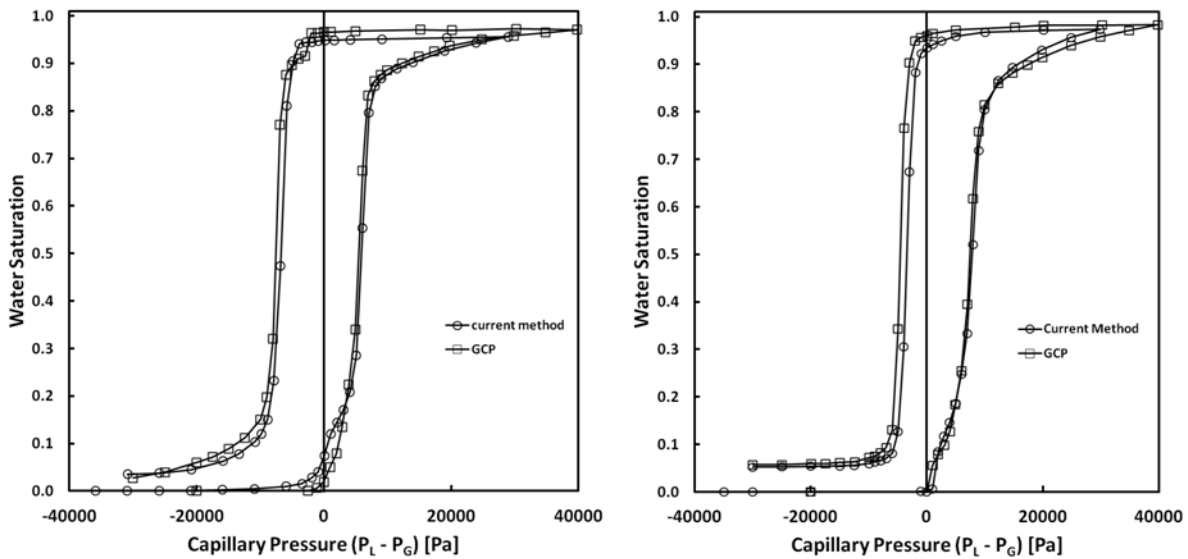
Figure 21: Pc-Sw curves for Toray090 using current method (Circles) and Using GCP (Squares): Toray090 10% PTFE (Left) and Toray090 20% PTFE (Right).

4.8.2. Difficulties Encountered During Method Development

4.8.3. Water Evaporation and Condensation

One problem encountered during the course of the experiment was evaporation and condensation of water inside the piping of the system at elevated temperatures. Fully humidified air inside the system is desirable to decrease the evaporation loss from the sample during the course of experiment; however, this can lead to condensation. A considerable effort was spent early on tracking down unknown issues at elevated temperatures that resulted in data as shown in Figure 22. The unexpected plateau on the withdrawal portion of the curve

indicated that either bubbles were evolving in the water piping preventing liquid from moving in and out of the sample, or water was condensing above the sample preventing changes in gas pressure from reaching the sample. After much trial and error, the latter proved to be the case and this was prevented by packing very fine glass beads in the piping above the sample to wick liquid water away from the area above the sample. The actual implementation of this approach required drilling larger holes in the top of the plug above the sample, as shown in Appendix B.8.
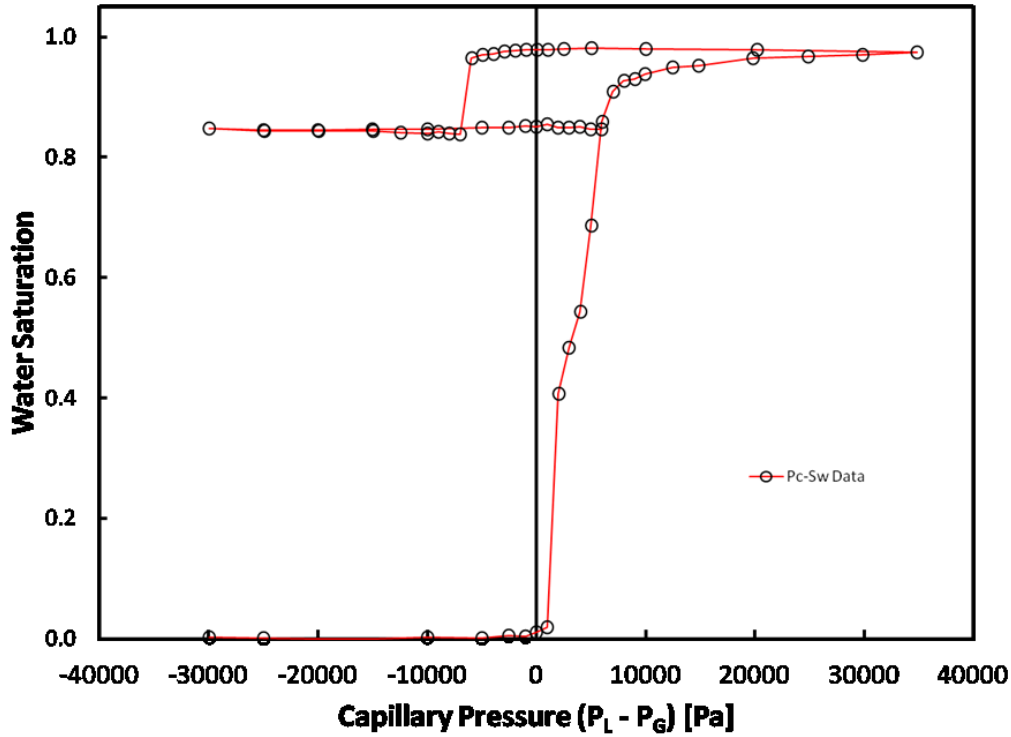
Figure 22: Capillary pressure curve obtained before utilising glass beads inside plug holes.

4.8.4. Apparent Sample Compression with Temperature

Another persistent problem was the apparent decrease in sample pore volume at increasing temperature as shown in Figure 23 (left). This problem also required significant effort to solve and is outlined here. The four leading explanations for this behavior were (i) thermal expansion of the vertical capillary which would mean the tube diameter used in Eq.(16) was changing, (ii) thermal expansion of the GDL material itself, (iii) the sample holder itself was undergoing thermal expansion leading to compression of the sample, (iv) the pressure sensor was not as thermally stable as hoped. The first possibility was ruled out by calculating the thermal expansion of stainless steel 304; the amount of dilation expected over the 60°C temperature

range used here would result in a 0.1% change in observed water volume compared to the 30% drop actually observed. The second possibility was also ruled out by using the filament analog model as described in Appendix E, which converts the total solid volume of the fibrous GDL into an equivalent long fiber with the same diameter. Thermal expansion calculations on this equivalent fiber indicate only 0.05% decrease in porosity of GDL over the range of 60K which is negligible compared to the 25% decrease in porosity is actually observed. The third possibility could not be ruled out by a similar calculation since the sample holder was made multiple different materials and had complex geometry. Instead tests were performed by removing the setscrew shown Figure 13, and placing a spring inside the compression cylinder to apply a constant force to the plug during the experiment. This resulted in the data in Figure 23 (right) which showed almost identical volume loss. Although this experiment did not identify the cause of the volume loss, it did rule out the possibility of sample compression. This is a very important result since it means that the actual sample volume is not changing, and the observed volume discrepancies are due to errors in the measurement of volume. Also, note that the plateaus in the high capillary pressure region of Figure 23 (right) are not totally flat. This is expected since the spring can give slightly when high pressures are applied. This indicates that the spring was not too stiff and was not itself causing compression of the sample.
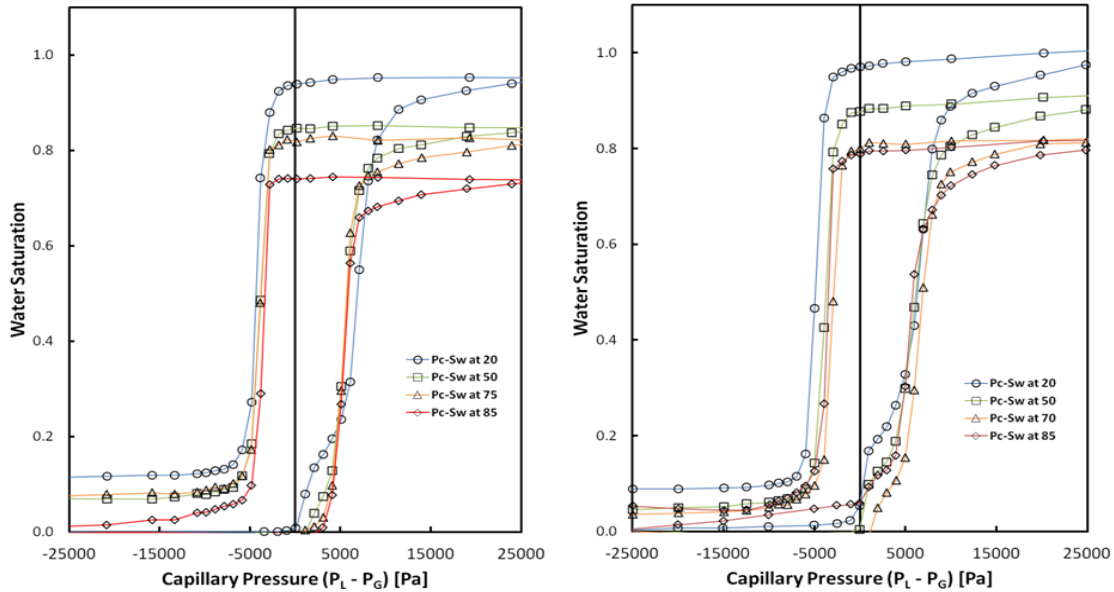
Figure 23: Capillary pressure curves for Toray090 10% PTFE at elevated temperatures using compression cylinder with set screw (Left) and compression cylinder with spring(Right).

The fourth option was finally investigated, and it was found that the pressure sensor used to monitor the relative change in height of a water column inside the capillary tube did not offer the thermal accuracy and stability claimed by the manufacturer. Figure 24 shows the results of heating the sensor from ambient to 75°C and recording the output voltage. The test was performed with a dry sensor and with a constant column of water above it. The two lines have slightly different slopes, and diverge at elevated temperatures. This is actually the opposite of the behavior seen in Figure 23, which indicates a smaller volume entering the sample at higher temperatures. For instance, if the true volume entering the sample is equal at 25°C and 85°C, then the voltage vs. temperature behavior given in Figure 24 would result in higher reported volume (since the voltage change is higher).
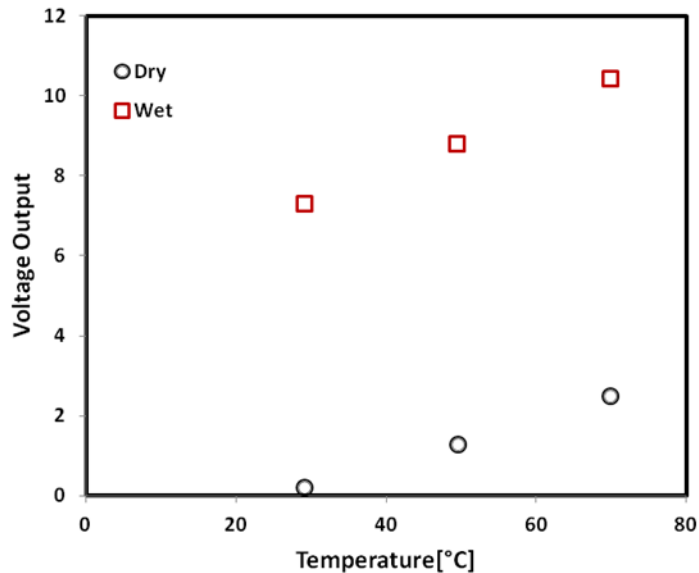
Figure 24: Calibration of differential pressure sensor at high temperatures.

Unfortunately, a satisfactory solution to the apparent reduction in pore volume has not been found at the time of this writing. In the data and results presented below the data are normalized relative to the maximum amount of water injected into the sample at each given temperature (i.e. all curves approach $S_w= 1$ at high P_C). This is justified based on the fact that sample compression was ruled out by using a spring to apply constant force on the sample,

rather than a setscrew which would transmit any thermal expansion of the sample holder to the sample.

4.9. GDM Materials

The materials used in this study were carbon fiber papers manufactured by Toray. The two types of materials lists (090 and 120) are basically identical in structure but differ in thickness (275 μm vs 385 μm for the 090 and 120 respectively). All of the treated Toray 090 samples were received from an industrial collaborator who added their own proprietary wettability treatments, which generally consist of adding varying amounts of PTFE emulsion and followed by drying and sintering. The concentration of the emulsion added controls the PTFE loading. One untreated Toray 090 sample (referred to as 090b) and all of the Toray 120 samples were received directly from the manufacturer, Toray Industries. The distinction between the 090 and 090b is important since these sample behaved much differently despite both being un-teflonated. Table 1 lists the properties of the samples that were studied. The uncompressed thickness of each sample was measured directly prior to testing using a micrometer (Mitutoyo) with 1 μm precision and 0.1 μm accuracy. Numerous tests were run on different samples to have a consistent data between the samples. The samples were tested as received by the suppliers unless otherwise noted.

Table 1: Physical Properties of Materials tested in this study

Brand	Model	PTFE loading [wt%]	Thickness [μm]	Porosity [m^3 m^{-3}]
Toray	120	0	385	0.77
		10	380	0.76
	090b	0	272	0.78
	090	0	272	0.78
		5	282	0.72
		10	277	0.71
		20	290	0.70

5. Results and discussion

5.1. Effect of PTFE Loading at Room Temperature

Figure 25 plots all the primary injection and withdrawal curves for Toray090 and Toray 120 with varying PTFE percentages by weight for direct comparison, with secondary curves omitted for clarity. The evidence of the PTFE addition is clearly visible in the direct comparison. As can be seen, with increasing PTFE both injection and withdrawal curves shift toward higher capillary pressures than the curves obtained for untreated samples. This indicates that more positive capillary pressure is required for water to penetrate into the pores of the hydrophobically treated samples, and similarly, less negative capillary pressure is required to withdraw water. The curves for the PTFE treated samples tend to cluster together and to converge into a single line, as do the untreated samples. Interestingly, the amount of PTFE added (by % weight) does not cause progressively more hydrophobic behavior, contrary to expectation. It is clear however, that the addition of PTFE does indeed render the GDMs more hydrophobic as expected. These observations agree with findings reported by Gostick et al[1]and others [4, 5].The difference in the withdrawal curves between treated and untreated GDLs also indicates that less pressure is required to withdraw water from treated samples and it is in fact easier to withdraw the water from treated sample than untreated GDL samples. The one main discrepancy in this data is the withdrawal pressure of the two untreated samples, which differ significantly from each other. The best explanation for this is that the Toray 090 was received from an industrial partner while the Toray 120 was received directly from Toray. Perhaps these materials were from different lots, or perhaps the industrial partner applied some pre-cleaning. Nonetheless the materials follow the overall trend that is seen in previous work and by other groups. This provides further confirmation that the present method is providing acceptable and expected results. It also confirms that the treated samples received from the partner company behave in a similar manner to other materials tested in the open literature despite the novel and proprietary techniques used to apply the PTFE coatings.
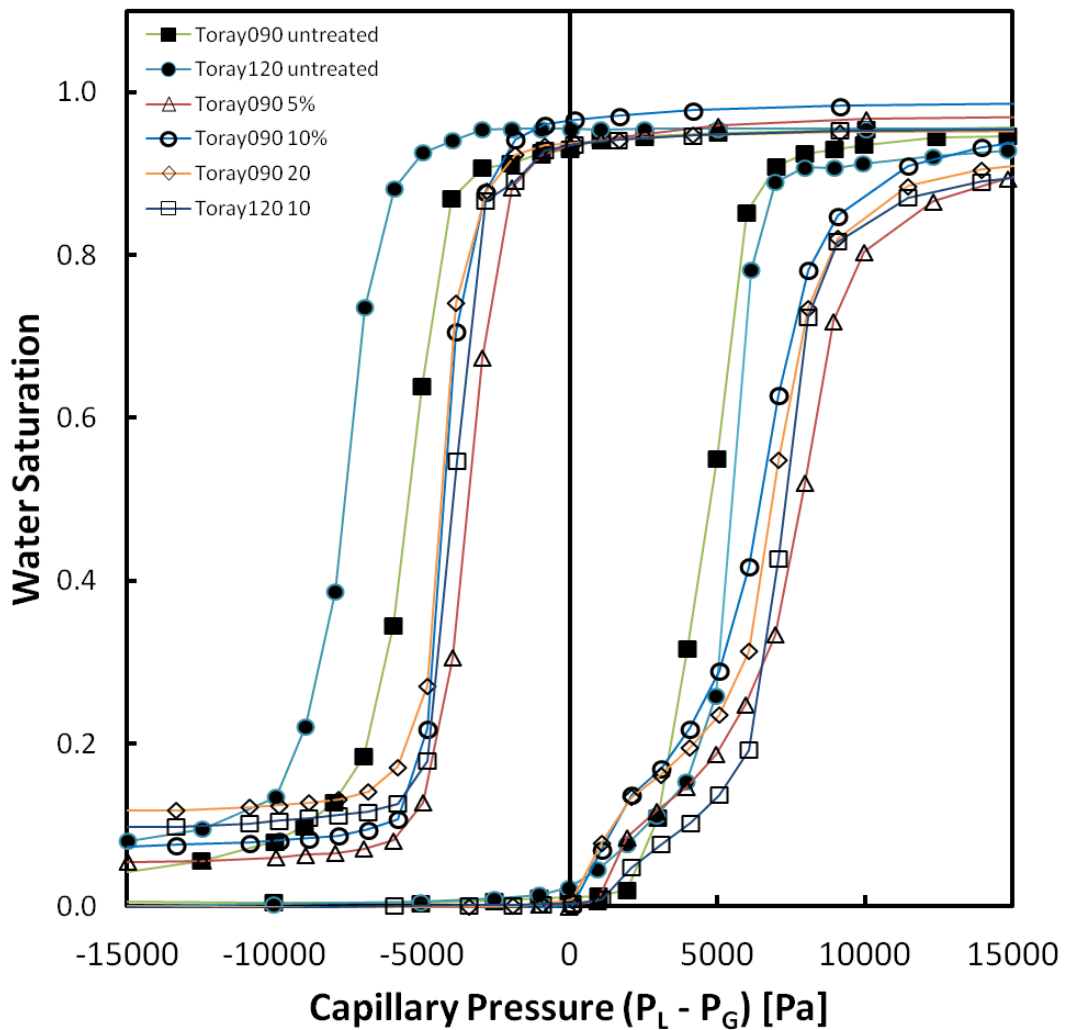
Figure 25: Primary injection and primary withdrawal curves for Toray090 and Toray 120 of Varying PTFE by weight %.

5.2. Untreated Samples at High Temperatures

One of the main objectives of this project is to measure capillary pressure curves in GDL electrodes at elevated temperatures. A compilation of the capillary pressure curves measured for the untreated Toray 120 and Toray 090b (received from supply rather than industrial partner) is given in Figure 26. Clearly, there are noticeable differences in capillary pressure curves measured at different temperatures. For the Toray 090b material shown Figure 26(right) there is a clear trend toward increasing capillary pressure with increasing temperature on the water invasion portion of the curve. The Toray 120 material in Figure 26(left) shows generally

similar behavior upon invasion, but the curves show less separation. Note that the Toray 090b tests were not performed at 50°C so this missing line might have coincided with the 25°C or 70°C and obscured the trend. Since surface tension decreases with increasing temperature and contact angle for graphite increases at a rate of 0.06°/°C [61], these two effects are working in opposite direction. Apparently, the very modest increase in contact angle between 25°C and 85°C has a large impact on the capillary behavior.
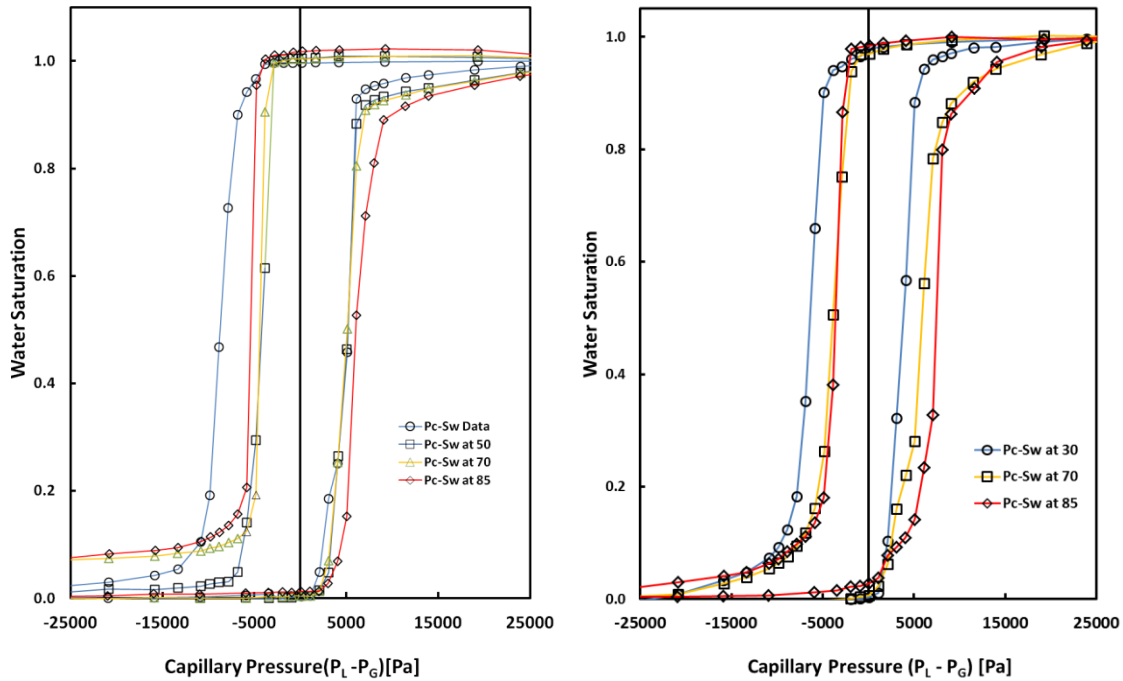
Figure 26: Capillary pressure curves for untreated GDLs at elevated temperatures. Left: Toray120 0% PTFE, Right: Toray090b 0% PTFE.

During withdrawal the both samples behave rather erratically. In both cases the 25°C line is significantly more negative than the other temperatures. Withdrawal curves at higher temperatures tend to cluster together, or in the case of the Toray 120 sample the 85°C curve moves to more negative pressures. She and Sleep saw similarly erratic behavior during water imbibition (i.e. analogous to water withdrawal in the present experiments) as shown in Figure 27 below. The dissimilar behaviour between invasion and withdrawal may be because of the different mechanism prevailing during invasion (water replacing air in GDL pores) versus withdrawal (air replacing water in GDL pores). Also, as described earlier in Section3.3, the

48

advancing contact angle is dominant during invasion and receding contact angle during withdrawal and these contact angles can in general behave differently with temperature[59], though data for water on graphite was not found.

One feature of that is apparent in Figure 26, is that the withdrawal curves at 25°C for both samples occur at much more negative pressure than the samples that have been heated. Repeat tests were performed on Toray 120 and 090b and the same behavior was observed. Since the tests are conducted in order of increasing temperature, this behavior suggests that something must change in the samples when heated to 50°C and above. To determine if exposure to hot water was the cause, a fresh sample was pretreated by boiling for 6 hours, then drying and testing. The large jump between 25°C and 50°C remained on the withdrawal portion. This result indicated that the testing procedure itself was not responsible for the change, but it is possible the pre-boiling was not a good facsimile for the conditions experienced during the test. A more detailed discussion of chemical alterations occurring to the sample during the course of the test is provided in Section 5.5.
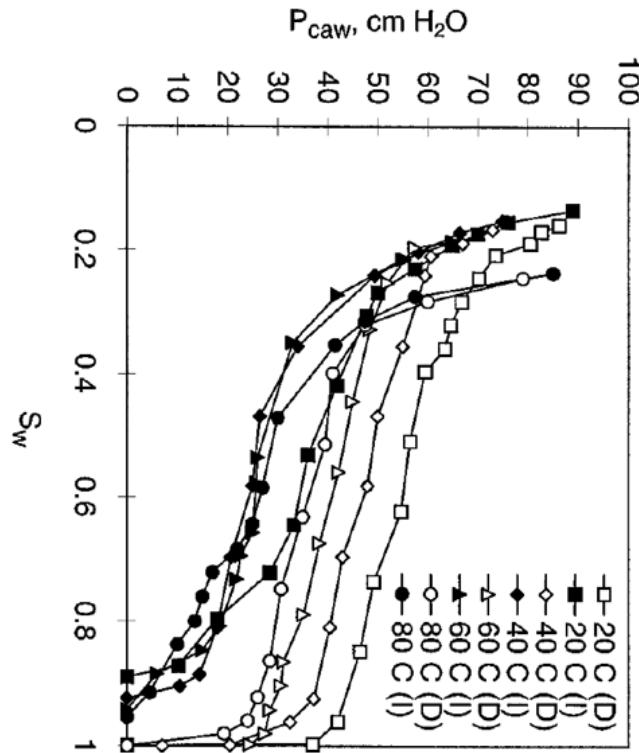

Figure 27: Temperature dependent capillary pressure curves of air and water in glass beads as reported by She and Sleep [8]. This graph has been rotated 90° to match the convention used in the present work with applied capillary pressure on the x-axis and non-wetting phase (air) saturation on the y-axis.

One unexpected result was obtained for untreated Toray 090 sample obtained from industrial partners as shown in Figure 28. The water invasion portion of the capillary pressure curves for this untreated sample behaved quite differently than the Toray 090b sample, with the curves shifting left at higher temperatures, rather than right. This behavior actually matched the results obtained with treated samples (as described in the next section), so it was initially thought that the samples must have been swapped during shipment. Thermo gravimetric analysis (TGA) confirmed, however, that no PTFE traces were present in the sample(TGA results are shown in Appendix D). It has been reported that graphitic surfaces can display a very wide range of wetting behaviors resulting from chemical alterations their surfaces [64]. The observed behaviour for this untreated sample may be due to some unknown treatment, pre-cleaning or other procedure that was applied to the sample by the industrial partner. The company was unable to disclose pre-treatment steps and procedures.
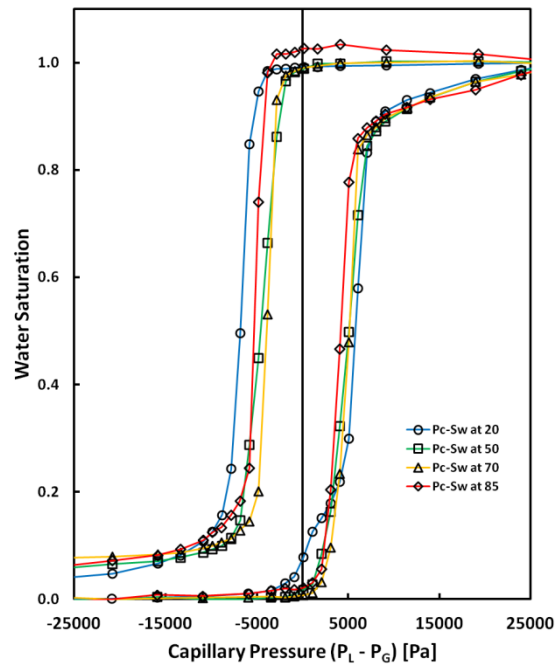
Figure 28: Capillary pressure curves for untreated Toray 090 received from industrial partners.

5.3. Treated Samples at High Temperatures

Capillary pressure curves for Toray120 10% PTFE and Toray 090 with 10% PTFE samples can be seen in Figure 29. The invasion portion of all capillary pressure curves shift left toward $P_C=0$ (lower capillary pressure) with temperatures. The direction of this shift agrees with the decrease in surface tension of water with temperature. Whether or not the magnitude of this shift can be explained by changing surface tension alone will be discussed in Section 5.4. Note that the contact angle of water on PTFE remains constant with temperature within the range of 25 - 100°C [58, 59,65] (See Figure 11). The very consistent and predictable behavior of these data can perhaps be attributed to the stabilizing influence of the PTFE coatings. Similar behaviour was observed for Toray 090 with 20% and 40% PTFE as shown on Figure 30.

During water withdrawal the capillary pressure curves for all the treated samples (with the exception of Toray 090 10% PTFE) overlap with each other very closely at all temperatures. Different behavior between injection and withdrawal were also observed for the untreated samples. This difference is likely due to differences in displacement mechanism. In basic terms, the invasion is controlled by throat sizes and is roughly described by the Washburn equation (Eq.(9)), while withdrawal is controlled by pore body size and many other factors including local fluid configurations, pore connectivity, throat aspect ratio, and so on. A detailed discussion of these effects is beyond the scope of this work.

One important point that can be noticed in Figure 29 and Figure 30 is that all the capillary pressure curves show some residual water after the water withdrawal step. It can also be observed that each subsequent curve at the next elevation in temperature begins at zero saturation. Since the samples were not removed from the device during the course of the test it must be explained why this resetting to zero occurs: Since the residual water is not connected to the water reservoir, once it evaporates from the sample it is not replaced. Hence during the period from the end of one experiment to the beginning of another (about 12 hours), the residual water clusters evaporate. It was confirmed that the sample was dry by removing a sample from the holder after 12 hours at 85°C and weighing it.
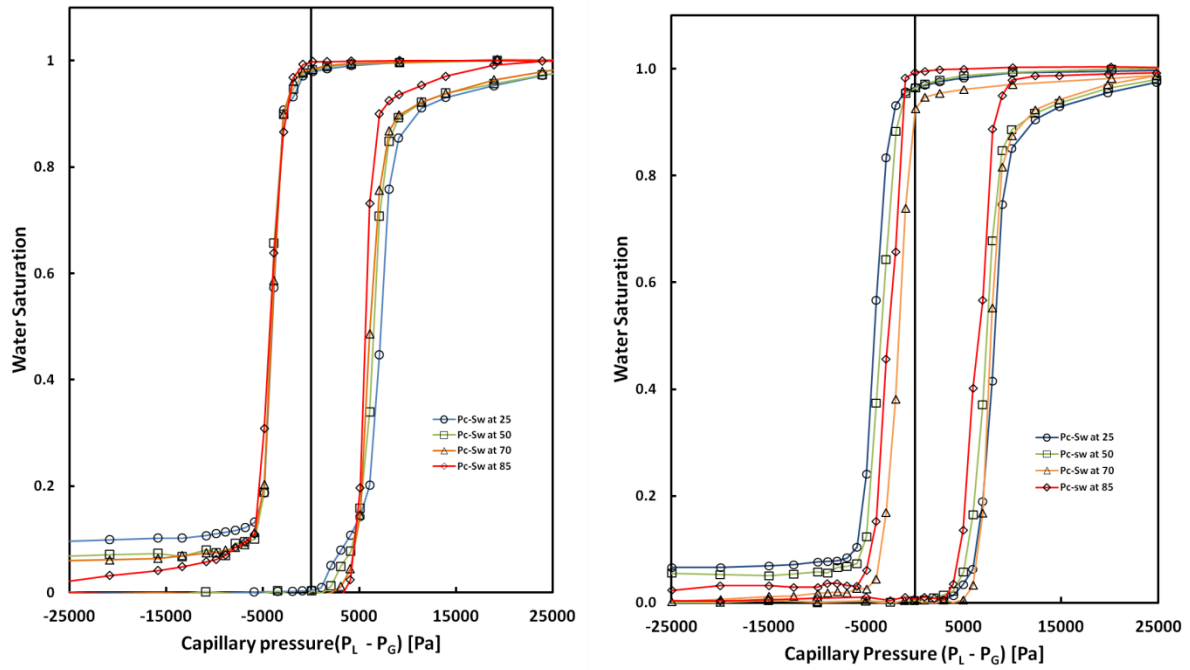
Figure 29: Capillary Pressure curves at elevated temperatures: Left: Toray 120 10%, Right: Toray 090 10%.
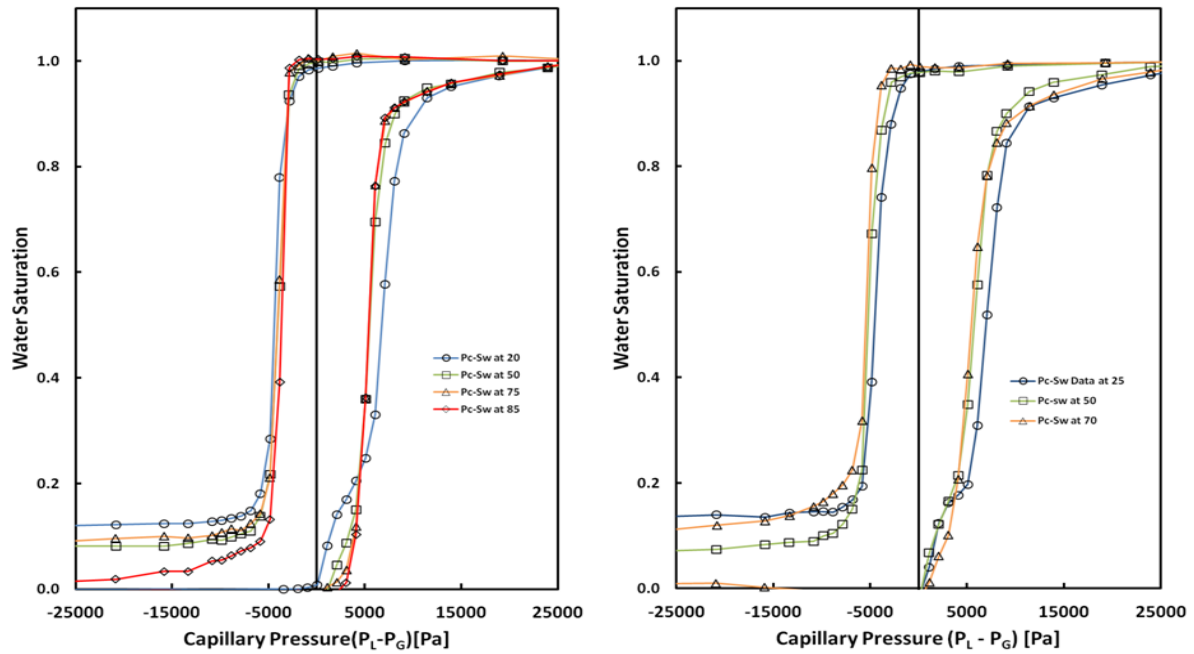

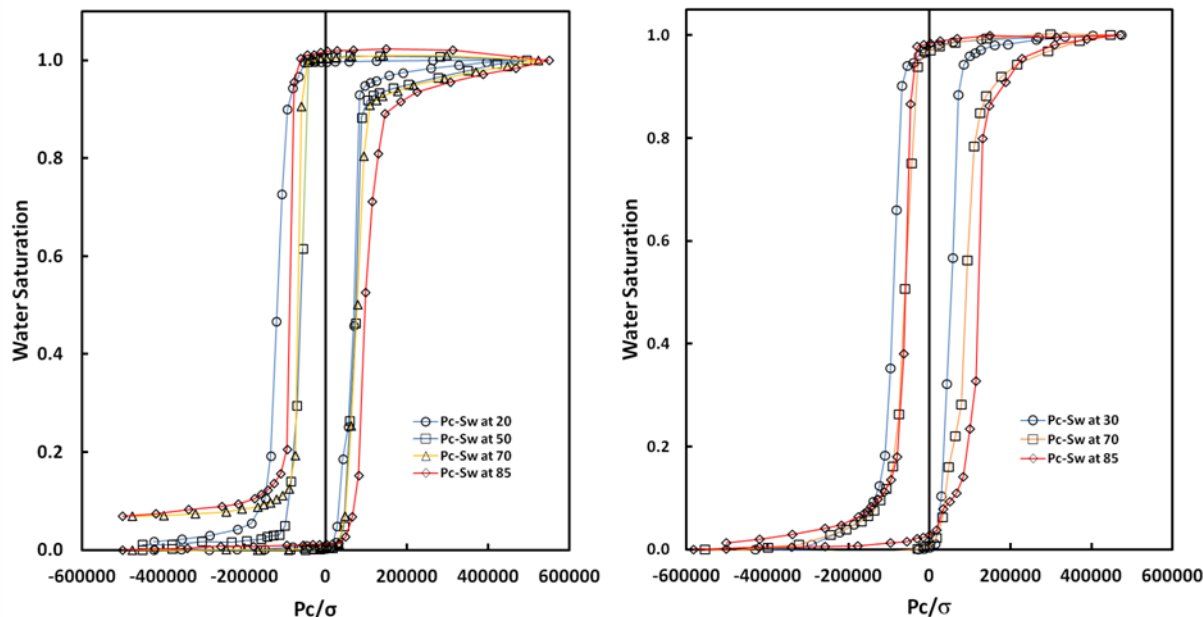**Figure 30: Capillary Pressure curves at elevated temperatures: Left: Toray090 20%, Right: Toray090 40%.**

5.4. Effect of Elevated Temperatures on Wettability

Aside from simply collecting high temperature capillary pressure data, one goal of this project was to assess the wettability changes, if any, of GDLs at elevated temperatures. In order to separate the impacts of changing wettability from changing surface tension, the experimentally measured capillary pressure values are normalized by the temperature dependent surface tension (referred as herein as σ-normalized curves) in accordance with the phenomenological behavior of the Laplace equation (Eq.(7)). After this treatment it is possible to plot P_c/σ vs. s_w data and any shifts between curves taken at different temperatures can be attributed to changing wettability.

Figure 31 shows σ-normalized capillary pressure curves for Toray120 and Toray 090b with 0% PTFE. Both graphs show shifts to the right for water invasion indicating that they are becoming slightly more hydrophobic when temperatures increase from room temperature to 85°C. If wettability is viewed in terms of contact angle, this behavior is in agreement with Fowkes and Harkins [61] who reported that contact angle of graphite increases slightly (by about 0.06°/°C or 3.6°) over the range up to 85°C.

The σ-normalization procedure yielded much more interesting results for the treated samples. Figure 32(left) shows the non-normalized data for Toray 120 with 10% PTFE by weight that was previously shown in Section 5.3. The injection curves showed a consistent trend toward lower capillary pressure at higher temperature, but it was not clear whether the magnitude of this shift was due to changing surface tension alone.   When the σ-normalization procedure is applied the results are shown in Figure 32(right). The injection curves all collapse, indicating that wettability does not change in the PTFE treated material with temperature. This behaviour disagrees with the measurements of Lim and Wang[11], who reported that the contact angle on the surface of FEP treated GDLs decreased with higher temperatures. On the other hand, it is well documented that the contact angle of water on PTFE is independent of temperature between 0 and 100°C[58, 59,65] so the present behavior might be expected in a PTFE coated

GDL matrix. It seems the differences in FEP and PTFE have significantly different wetting properties despite their similar chemical structure.

Figure 31: Capillary pressure curves normalized by the temperature dependent surface tension of water. (Left) Toray120 with 0% PTFE by wt, (right) Toray 090b with 0% PTFE by wt.

Before the σ-normalization is applied the withdrawal portion of the curves coincide almost exactly shown in Figure 32(left). Once the σ-normalization is applied there is a small change towards more negative values of P_C/σ with increasing temperature but this is very minimal. The withdrawal curves are closer to zero capillary pressure, so their values are not as significantly shifted. Also of note is the fact that the withdrawal curves do not show the large jump between 25 and 50 °C as was observed in the untreated materials (Figure 31). This suggests that pre-cleaning, sintering or some other factor related to the coating process may alter the treated GDLs.

To confirm the results of the σ-normalization, tests were run for Toray 090 of varying PTFE at different temperatures. Figure 33 shows the σ-normalized capillary pressure curves for Toray 090 10% (left) and Toray 090 20% (right). Again, the P_C/σ curves are very tightly bunched for

both the samples in agreement with the behaviour for Toray 120 10% PTFE. The consistent behaviour observed for treated sample confirms that GDL wettability actually remains unchanged with temperature.
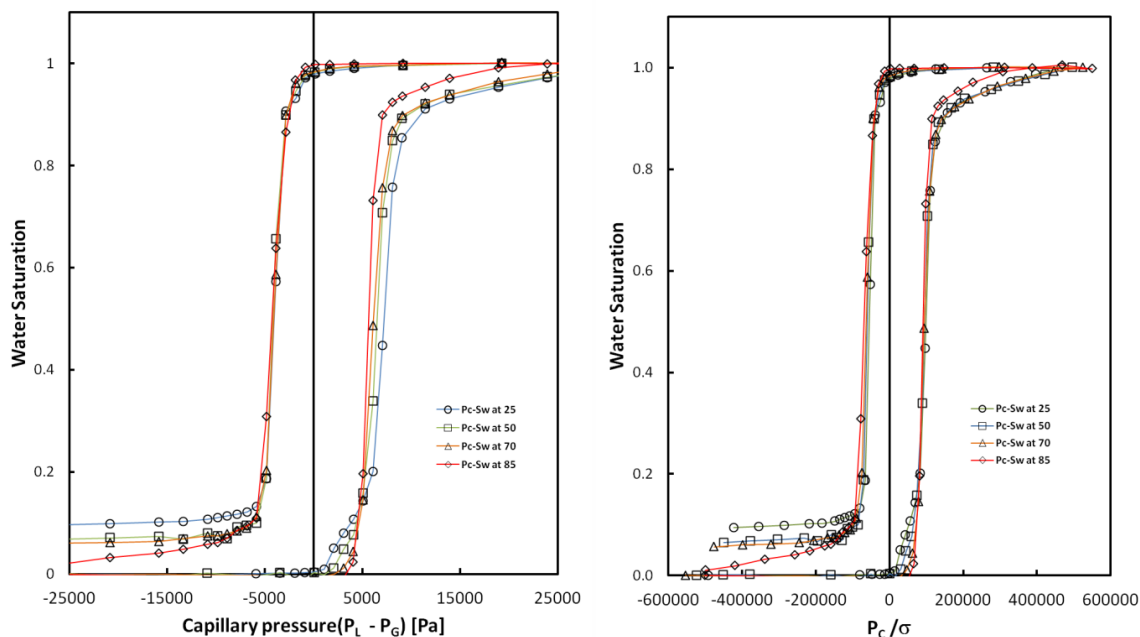

Figure 32: Toray120 with 10% PTFE by Wt, Left: Capillary pressure curves at elevated temperatures between 25°C to 85°C. Right: Capillary Pressure curves normalized by temperature dependent surface tension of water.
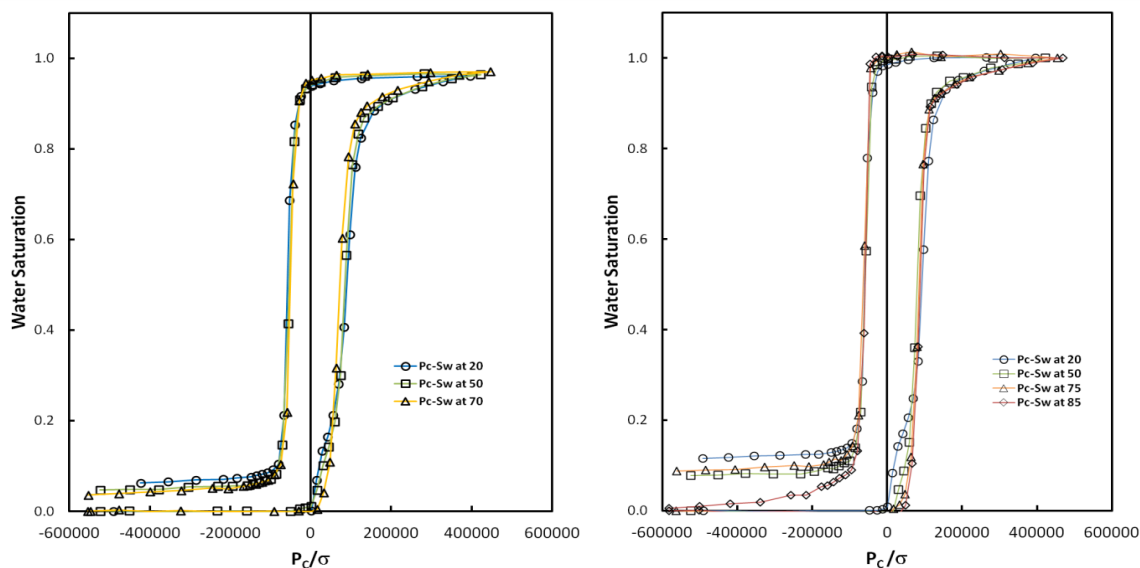

Figure 33:Capillary pressure curves when normalized with temperature dependent surface tension of water. Left: Toray090 10% PTFE and Right: Toray090 20% PTFE.

5.4.1. Wettability Index on σ-Normalized Capillary Curves

Instead of determining whether curves are shifting or not by visual inspection it is desirable to apply some sort of quantitative metric. The US Bureau of Mines has proposed a wettability index (I_{USBM}) that has been successfully applied to GDL materials in the past [1]. The I_{USBM} is defined as follows:

$$I_{USBM} = \log\left(\frac{A_1}{A_2}\right)$$

(20)

where A_1 is the area between the y-axis and the withdrawal curve, and A_2 is the area between the y-axis and the injection curve. $I_{USBM} < 0$ indicates a hydrophobic material and vice-versa. For instance, in hydrophobic materials curves are shifted to the right and the area of A_2 is larger than A_1 leading to $I_{USBM} < 0$. This analysis was performed on all of the σ-normalized samples presented above and the results are given in Figure 34. These values show quite a lot of scatter, but the general trends are visible. The untreated samples move from hydrophilic at room temperature to hydrophobic at elevated temperatures (i.e. the I_{USBM} values move from positive to negative). Although this is in agreement with the general shift towards higher pressure required for invasion, it must be noted that most of this change is due to fact that the withdrawal curves at these two temperatures shifted significantly thereby reducing the value of A_1 in Eq.(20) (rather than increasing A_2). The Toray 090b data do show a consistently decreasing I_{USBM} value in agreement with the shifts seen in invasion capillary pressure for that sample (Figure 26). The treated samples are plotted in Figure 34(right). Almost all I_{USBM} values lie below 0 as expected for PTFE treated samples, and they are mostly flat which agrees with the fact that all the σ-normalized curves coincide quite closely.
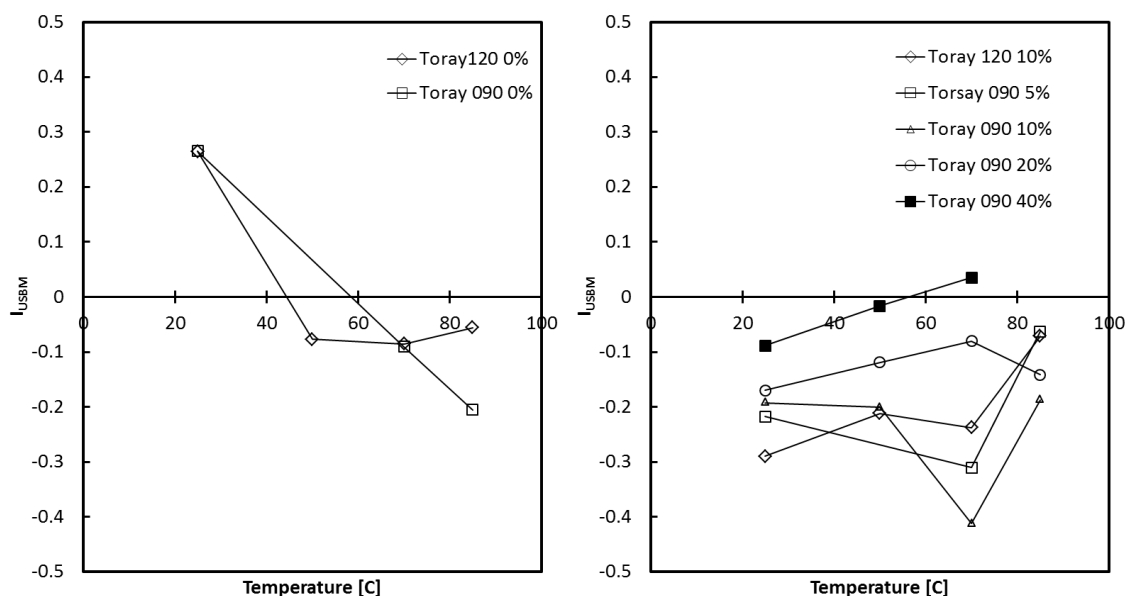
Figure 34: I_{USBM} **values calculated on the** σ**-normalized curves. Left: untreated samples, right: treated samples.**

5.5. Investigation of Chemical Effects

5.5.1. Pre-Treatment of Samples

Samples have been generally tested as received from the suppliers, but some limited pre-treatment tests have been performed to investigate the variation in measured capillary behaviour. Specially, some GDL samples have boiled for at least 6 hrs and dried overnight in an oven before testing. Interestingly, the capillary pressure test shows that there is no variation in measured behaviour due to such treatment as shown in Figure 35. It would have been worthwhile to perform other more vigorous pre-treatment and pre-cleaning steps such as acetone or boiling in H_2SO_4 solution, but time did not permit this. Pre-boiling in water was intended to provide a close facsimile to the actual conditions in the sample holder, but it must be noted that during boiling the sample was not interacting with oxygen since it was completely submerged. In the actually test the sample is partially saturated and in constant contact with oxygen in the air and water, so if oxidation is important then this pre-treatment may not be as representative as hoped. Future work in this area should attempt (a) bubble oxygen in the boiling water and (b) performing the capillary pressure test with inert N_2 rather than air.
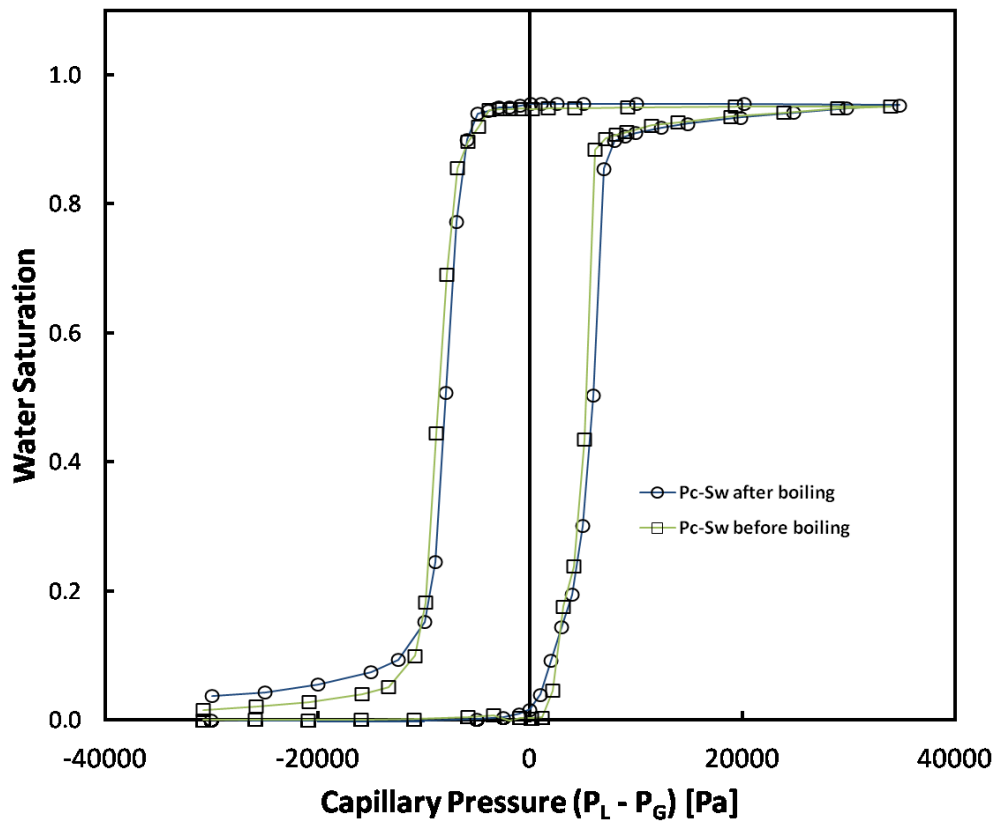
Figure 35: Capillary pressure curve for Toray120 0% PTFE before and after pre-treatment.

5.5.2. Impact of Decreasing Temperature

The data presented in the above sections were taken on a given sample as the temperature was increased from room to 85°C. Some trends were seen and these were interpreted in terms of changing surface tension and temperature dependent contact angles. In order to confirm that these effects were real, a series of tests were conducted in which the temperature was progressively lowered from 85°C back to room temperature. The intention was to determine if the observed changes were reversible, as they should be if surface tension and contact angle effects alone were responsible, or if some other factor was at work such as chemical alteration of the water or sample. Figure 36 shows the capillary pressure curves taken at the same temperature on the heating and cooling paths (see Figure 19 for more details about the temperature protocol). As can be seen there appears to be some irreversibility. The data at 70°C coincide almost perfectly, but the 50° and 20°C data deviate. This irreversibility may be

due to chemical alteration of GDL or may be due to the contamination of experimental water during the course of experiment. These investigations are explained in detail in the following sections.
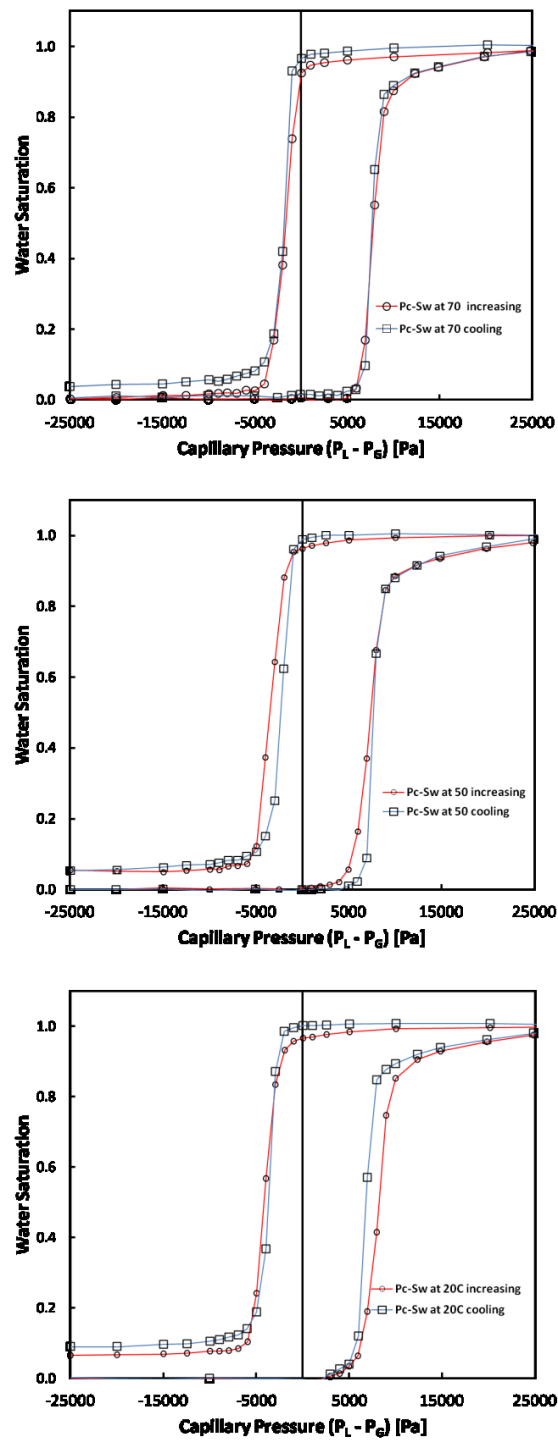

Figure 36: Comparisons of capillary pressure curves measured at increasing and decreasing temperatures for Toray090 10% PTFE.

5.5.3. Contamination of Experimental Water

It is possible that at high temperature ions could be leached from stainless steel piping, gasket material in sample holder, and from the carbon and PTFE of the GDL itself. It is well documented that the surface tension and contact angle of water is affected due to the leaching of ions [66-68]. Many experiments had illustrated that the addition of most inorganic salts to water raises the surface tension noticeably at salt concentrations above 0.01M. Several authors[69, 70]have reported a slight increase in the contact angle of water on paraffin wax, PTFE and polyethylene with increasing NaCl concentration. In contrast, many other reports[68][71, 72] indicate no change of water contact angle on polymer surfaces irrespective of ion concentration. In any event, it was deemed worthwhile to measure the ion concentration in the system water after tests were performed to detect any contamination. Inductively coupled plasma(ICP) mass spectrometry was used to measure the concentration of many ions of interest, and the results are plotted in Figure 37.

Ions concentrations indicated at 20°C in Figure 37 are a blank sample of deionized (DI) water. It is surprising to see a non-negligible nickel concentration in the standard DI water; however most of the other ions are at zero. The 50°C sample was lost due to a sampling error. Many ions appeared in the water when the temperature was increased to 70°C, especially iron (Fe2599), molybdenum (Mo2020), sulfur (S1802) and Silica (Si2516). For many of these, concentrations appear to decrease at 80°C except sulphur which increased substantially. The presence of sulphur is unexpected since Viton and PTFE gaskets were used throughout the setup, and no silicone rubber was used. As temperature was decreased, many of the ions seem to reappear at 70°C. When temperature is decreased to 50°C, most other ions seem to be very minimal, however the concentration of manganese increased slightly and nickel remain almost constant. Concentration of manganese decreases when temperature decreases to 30°C. Most of the other ions are at zero.

The ICP analysis confirms that some ions actually did leach from piping and fittings and may be from GDL materials. However, the concentrations of the ions are so small that it is unlikely that changes in surface tension are responsible for the observed discrepancies. Measuring the variation of surface tension due to ions in water at different temperature is beyond the scope of this project. Future embodiments of the device might want to consider glass tubing or some other inert coating on the piping to forestall any ionic contamination.
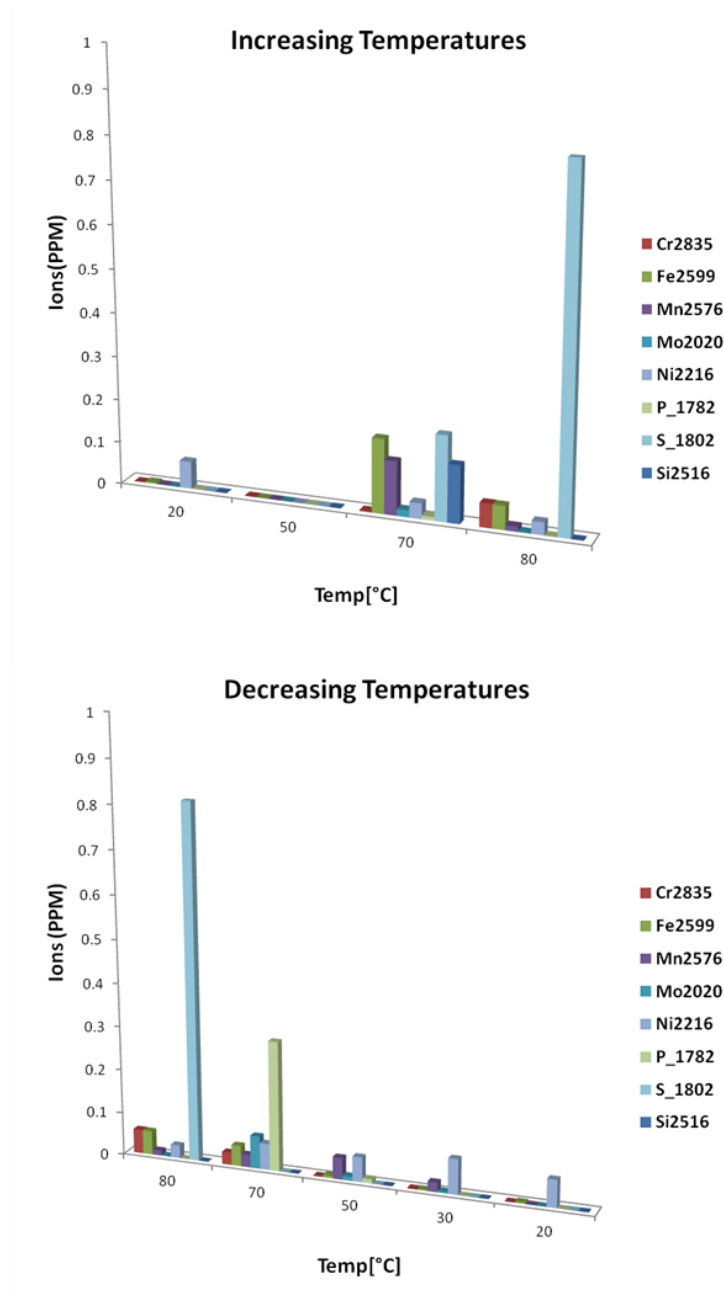

Figure 37:Inductively Coupled Plasma(ICP) analysis at increasing and decreasing temperatures.

5.5.4. Chemical Alteration of GDL Surfaces

The observed irreversibility may also be due to the chemical alteration of GDL sample during the course of the experiment. To investigate, different samples of GDLs (with or without PTFE) are boiled in de-ionized water for 12 hrs and dried. Several surface analysis techniques were employed in an attempted to detect before and after differences in the surface composition. Firstly, Fourier transform infrared spectroscopy (FTIR) was performed to compare new (never boiled samples) to a boiled sample. Figure 38 shows the spectra of 4 different materials. The top row is for untreated Toray 090 and this curve shows almost not features. The second and third rows are for treated Toray 090 with 10 and 20% PTFE respectively. These data show a feature at about 1200 cm^{-1} which corresponds to the PTFE. The bottom row shows Toray 090 with 20% PTFE that has been boiled for 6 hours. A small feature can be discerned at 1600 cm^{-1} that corresponds to some sort of carbon functionalization. This seems like fairly strong evidence that the carbon substrate material did indeed undergo some sort of chemical alteration when boiled, although it must be pointed out that the capillary pressure test on pre-boiled Toray 090 (untreated) did not show any changes.
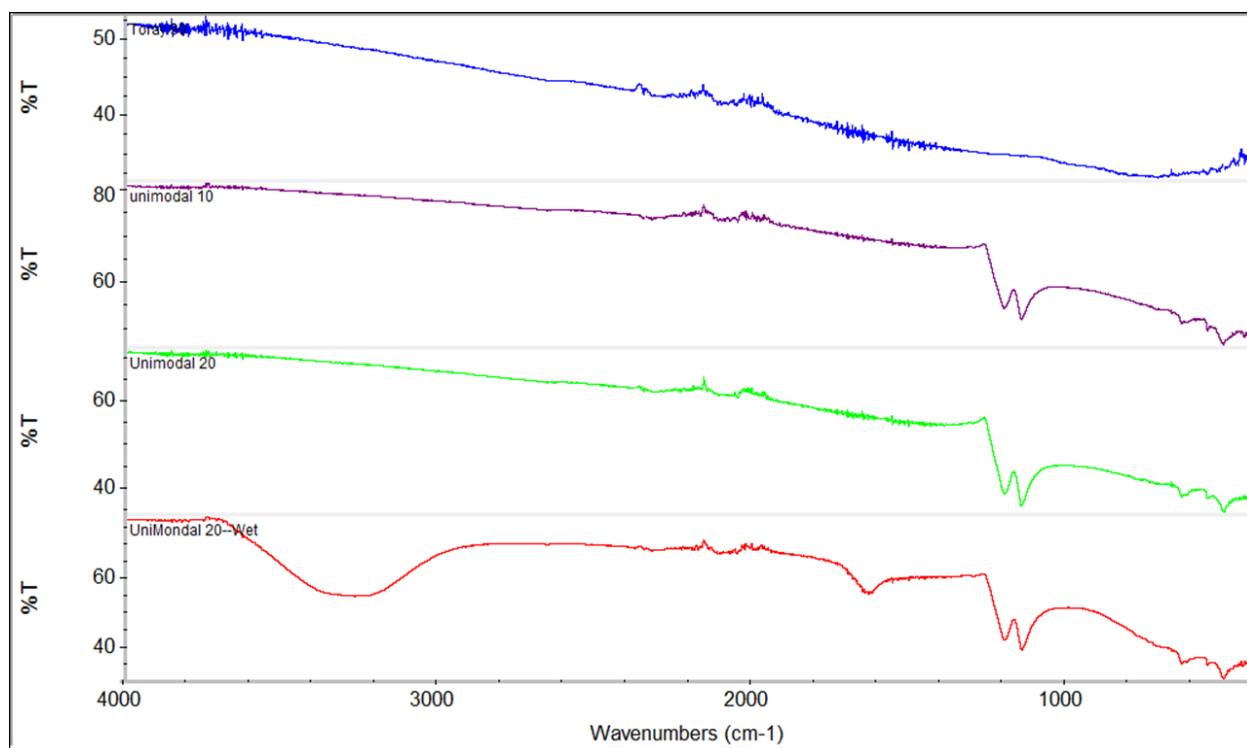
Figure 38:FTIR spectra for 4 samples from top to bottom: dry Toray 090, dry Toray 090 10%, dry Toray 090 20% and boiled Toray 090 20%.

A much more in-depth study of chemical changes is required, but this was beyond the scope of the present work. Several suggestions pursuing this work are given in the Conclusion section.

6. Conclusions

A device for measuring air-water capillary pressure curves of GDLs at elevated temperatures was constructed. The main modification of this device over those previously reported was the use of a vertical capillary tube and high accuracy differential pressure sensor to measure water uptake rather than an analytical balance or syringe pump. This allowed the placement of the entire apparatus inside an oven for temperature control.

Using the described method capillary pressure curves of various GDLs were measured at various temperatures between 25°C and 85°C. It was found that the capillary pressure curves of GDL materials are moderately sensitive to temperature. In their work on water-silica sand systems, She and Sleep [8]saw non-wetting phase injection curves move towards P_C = 0 when temperature was increased. In the present work, untreated GDLs did not follow that trend, and the capillary pressure curve actually shifted away from P_C = 0, however the results are somewhat erratic. This shift toward higher capillary pressures agrees with the increasing contact angle of water on graphite[61], but the increase is modest and it is somewhat surprising that this was sufficient to overcome the effect of decreasing surface tension. During water withdrawal, the curves did not follow any observable trend. When treated with a PTFE coating, GDLs behaved in an opposite manner with capillary pressure moving toward P_C = 0 during injection with temperature. Shifts in this direction correspond to the changing surface tension of water at elevated temperatures. The contact angle of water of pure PTFE surfaces is almost perfectly stable between 25°C and 85°C [58, 59, 65], and the presence of PTFE in the samples seems to reflect this.

In order to determine if observed changes in capillary pressure curves were due to temperature sensitive surface tension or changing wettability, the data was normalized by the surface tension. Any shifts in this σ-normalized data with temperature could be attributed to changing wettability. The untreated samples showed widely varying behavior, indicating that the pure graphite surfaces do change in wettability with temperature (although as summarized in the following paragraph this may be due to chemical alterations). The curves for the treated

samples however, all coincided very closely after this σ-normalization was applied. This behavior could be attributed to the stable contact angle of water on PTFE surfaces.

Several of the results obtained in this work suggested that chemical alterations to either the sample or the water were occurring. For instance, the water withdrawal curves for untreated samples differed significantly when heated from 25°C to 50°C, but no further changes were observed when the temperature was raised to 70°C or 85°C. Pre-boiling samples did not eliminate this effect which suggested that the effect was not due to the testing conditions, but the lack of oxygen contact with the sample during the pre-boiling might have been significant. To further investigate the chemical alterations, some tests were performed on cooling the samples. It was found that the curves were not fully reversible, which again indicates some chemical changes were occurring. The water in the system was investigated for ion contamination from the piping and gasket. Some increase in ions concentration was found in the heated samples, but the levels were much too low to impact surface tensions or wettability. FTIR analysis of the GDL surface indicated that some small chemical change related to carbon functionalization was present on boiled samples.

Future work should include:

- The measured pore volume of the samples continually decreased with increasing temperature. It was unclear why this occurred but efforts were made to demonstrate that it was not due to sample compression. Most likely this was caused by unexpectedly poor thermal stability of the differential pressure sensor. Attempts were made to measure the sensor's instability, but these were inconclusive. It is recommended that the setup be adjusted such that only the sample holder is heated, and not the sensor to avoid this issue.
- The chemical alteration of the GDL during the tests was a problem. It is suggested that an inert gas such as N_2 be used as the non-wetting phase rather than air. This would prevent any oxidation of the GDL during the test, which may or may not resolve the observed irreversibility.

- Several different test protocols should be tried in order to help obtain more consistent results. Samples should be pretreated in a consistent way, such as a boiling in acetone, or H_2SO_4 to help cleanse the surfaces. In this way all samples start from a similar condition. Also, tests should be run on samples starting at different temperatures rather than starting them all at 25°C and increasing. This would elucidate some of the problems concerning the withdrawal curves varying so widely.

- Chemical analysis of all samples should be performed before and after each test. In the present work FTIR analysis was only performed on pre-boiled samples, but this was perhaps not a reliable simulation of the actual test conditions. A thorough and detailed surface chemistry study is required.

7. References

1.	Gostick, J.T., et al., *Wettability and capillary behavior of fibrous gas diffusion media for polymer electrolyte membrane fuel cells.* Journal of Power Sources, 2009. **194**(1): p. 433-444.
2.	Gostick, J.T., et al., *Characterization of the Capillary Properties of Gas Diffusion Media Modeling and Diagnostics of Polymer Electrolyte Fuel Cells*, C.-Y. Wang and U. Pasaogullari, Editors. 2010, Springer New York. p. 225-254.
3.	Fairweather, J.D., *A microfluidic approach for measuring capillary pressure in PEMFC gas diffusion layers.* Electrochemistry communications, 2007. **9**(9): p. 2340.
4.	Fairweather, J.D., *The effects of wetproofing on the capillary properties of proton exchange membrane fuel cell gas diffusion layers.* Journal of Power Sources, 2010. **195**(3): p. 787.
5.	Harkness, I.R., *The use of a novel water porosimeter to predict the water handling behaviour of gas diffusion media used in polymer electrolyte fuel cells.* Journal of Power Sources, 2009. **193**(1): p. 122.
6.	Bachmann, J. and R.R. van der Ploeg, *A review on recent developments in soil water retention theory: interfacial tension and temperature effects.* Journal of Plant Nutrition and Soil Science, 2002. **165**(4): p. 468.
7.	Sinnokrot, A., *Effect of temperature level upon capillary pressure curves.* Old SPE Journal, 1971. **11**(1): p. 13-22.
8.	She, H.Y., *The effect of temperature on capillary pressure-saturation relationships for air-water and perchloroethylene-water systems.* Water resources research, 1998. **34**(10): p. 2587.
9.	Dullien, F.A.L., *Porous media: fluid transport and pore structure*. Vol. 2. 1992: Academic press San Diego.
10.	Mason, G., *Capillary behavior of a perfectly wetting liquid in irregular triangular tubes.* Journal of colloid and interface science, 1991. **141**(1): p. 262.
11.	Lim, C., *Effects of hydrophobic polymer content in GDL on power performance of a PEM fuel cell.* Electrochimica Acta, 2004. **49**(24): p. 4149.
12.	Carrette, L., K. Friedrich, and U. Stimming, *Fuel cells–fundamentals and applications.* Fuel cells, 2001. **1**(1): p. 5-39.
13.	Wilson, M.S., J.A. Valerio, and S. Gottesfeld, *Low platinum loading electrodes for polymer electrolyte fuel cells fabricated using thermoplastic ionomers.* Electrochimica Acta, 1995. **40**(3): p. 355-363.
14.	Wilkinson, G.E. and A. Klute, *The temperature effect on the equilibrium energy status of water held by porous media.* Soil Science Society of America Journal, 1962. **26**(4): p. 326-329.
15.	Mennola, T., et al., *Measurement of ohmic voltage losses in individual cells of a PEMFC stack.* Journal of Power sources, 2002. **112**(1): p. 261-272.
16.	Inthamoussou, F.A., R.J. Mantz, and H. De Battista, *Flexible power control of fuel cells using sliding mode techniques.* Journal of Power Sources, 2012.

17.   Wood, D.L., J.S. Yi, and T.V. Nguyen, *Effect of direct liquid water injection and interdigitated flow field on the performance of proton exchange membrane fuel cells.* Electrochimica Acta, 1998. **43**(24): p. 3795-3809.

18.   Yan, Q., H. Toghiani, and J. Wu, *Investigation of water transport through membrane in a PEM fuel cell by water balance experiments.* Journal of Power Sources, 2006. **158**(1): p. 316-325.

19.   Karimi, G. and X. Li, *Electroosmotic flow through polymer electrolyte membranes in PEM fuel cells.* Journal of Power Sources, 2005. **140**(1): p. 1-11.

20.   Spernjak, D., A.K. Prasad, and S.G. Advani, *Experimental investigation of liquid water formation and transport in a transparent single-serpentine PEM fuel cell.* Journal of Power Sources, 2007. **170**(2): p. 334-344.

21.   Park, J., et al., *Neutron imaging investigation of liquid water distribution in and the performance of a PEM fuel cell.* International Journal of Hydrogen Energy, 2008. **33**(13): p. 3373-3384.

22.   Springer, T.E., T. Zawodzinski, and S. Gottesfeld, *Polymer electrolyte fuel cell model.* Journal of the Electrochemical Society, 1991. **138**(8): p. 2334-2342.

23.   Bernardi, D.M. and M.W. Verbrugge, *Mathematical model of a gas diffusion electrode bonded to a polymer electrolyte.* AIChE journal, 1991. **37**(8): p. 1151-1163.

24.   Natarajan, D. and T. Van Nguyen, *A two-dimensional, two-phase, multicomponent, transient model for the cathode of a proton exchange membrane fuel cell using conventional gas distributors.* Journal of the Electrochemical Society, 2001. **148**(12): p. A1324-A1335.

25.   Fuller, T.F. and J. Newman, *Water and thermal management in solid-polymer-electrolyte fuel cells.* Journal of the Electrochemical Society, 1993. **140**(5): p. 1218-1225.

26.   Tüber, K., D. Pócza, and C. Hebling, *Visualization of water buildup in the cathode of a transparent PEM fuel cell.* Journal of Power Sources, 2003. **124**(2): p. 403-414.

27.   Pekula, N., et al., *Study of water distribution and transport in a polymer electrolyte fuel cell using neutron imaging.* Nuclear Instruments and Methods in Physics Research Section A: Accelerators, Spectrometers, Detectors and Associated Equipment, 2005. **542**(1): p. 134-141.

28.   Barbir, F., H. Gorgun, and X. Wang, *Relationship between pressure drop and cell resistance as a diagnostic tool for PEM fuel cells.* Journal of Power Sources, 2005. **141**(1): p. 96-101.

29.   Cindrella, L., et al., *Gas diffusion layer for proton exchange membrane fuel cells—A review.* Journal of Power Sources, 2009. **194**(1): p. 146-160.

30.   Mathias, M., et al., *Diffusion media materials and characterisation.* Handbook of fuel cells, 2010.

31.   Gostick, J.T., et al., *On the role of the microporous layer in PEMFC operation.* Electrochemistry Communications, 2009. **11**(3): p. 576-579.

32.   Gostick, J.T., et al., *In-plane and through-plane gas permeability of carbon fiber electrode backing layers.* Journal of power sources, 2006. **162**(1): p. 228-238.

33.   Escribano, S., et al., *Characterization of PEMFCs gas diffusion layers properties.* Journal of power sources, 2006. **156**(1): p. 8-13.

34.   Williams, M.V., et al., *Characterization of gas diffusion layers for PEMFC.* Journal of The Electrochemical Society, 2004. **151**(8): p. A1173-A1180.

35. Bevers, D., R. Rogers, and M. Von Bradke, *Examination of the influence of PTFE coating on the properties of carbon paper in polymer electrolyte fuel cells.* Journal of power sources, 1996. **63**(2): p. 193-201.

36. Chang, H.M., et al., *Optimization of polytetrafluoroethylene content in cathode gas diffusion layer by the evaluation of compression effect on the performance of a proton exchange membrane fuel cell.* Journal of power sources, 2011. **196**(8): p. 3773-3780.

37. Park, S. and B.N. Popov, *Effect of cathode GDL characteristics on mass transport in PEM fuel cells.* Fuel, 2009. **88**(11): p. 2068-2073.

38. Jasper, J.J., *The surface tension of pure liquid compounds.* 1972.

39. Kwok, D. and A. Neumann, *Contact angle measurement and contact angle interpretation.* Advances in Colloid and Interface Science, 1999. **81**(3): p. 167-249.

40. Grant, S.A. and A. Salehzadeh, *Calculation of Temperature Effects on Wetting Coefficients of Porous Solids and Their Capillary Pressure Functions.* Water Resour. Res., 1996. **32**(2): p. 261-270.

41. Bikerman, J., *Surface Energy of Solids.* physica status solidi (b), 1965. **10**(1): p. 3-26.

42. De Vries, D.A., *The theory of heat and moisture transfer in porous media revisited.* International journal of heat and mass transfer, 1987. **30**(7): p. 1343-1350.

43. Grant, S.A. and J. Bachmann, *Effect of temperature on capillary pressure.* GEOPHYSICAL MONOGRAPH-AMERICAN GEOPHYSICAL UNION, 2002. **129**: p. 199-212.

44. Gardner, R., *Relation of temperature to moisture tension of soil.* Soil Science, 1955. **79**(4): p. 257.

45. Okandan, E., *The effect of temperature and fluid composition on oil-water capillary pressure curves of limestone and sandstones and measurement of contact angle at elevated temperatures.* 1973: Dept. of Petroleum Engineering, Stanford University.

46. Jury, W.A., *Simultaneous transport of heat and moisture through a medium sand.* 1973: University of Wisconsin--Madison.

47. Chahal, R., *Effect to Temperature and Trapped Air on Matric Suction.* Soil Science, 1965. **100**(4): p. 262.

48. Constantz, J., *Comparison of isothermal and isobaric water retention paths in nonswelling porous materials.* Water Resources Research, 1991. **27**(12): p. 3165-3170.

49. Nimmo, J. and E. Miller, *The temperature dependence of isothermal moisture vs. potential characteristics of soils.* Soil Science Society of America Journal, 1986. **50**(5): p. 1105-1113.

50. Anderson, W.G., *Wettability literature survey-part 4: Effects of wettability on capillary pressure.* Journal of Petroleum Technology, 1987. **39**(10): p. 1283-1300.

51. Marmur, A., *Equilibrium contact angles: theory and measurement.* Colloids and Surfaces A: Physicochemical and Engineering Aspects, 1996. **116**(1): p. 55-61.

52. Wenzel, R.N., *Surface Roughness and Contact Angle.* The Journal of Physical Chemistry, 1949. **53**(9): p. 1466-1467.

53. Cassie, A. and S. Baxter, *Wettability of porous surfaces.* Transactions of the Faraday Society, 1944. **40**: p. 546-551.

54. Adamson, A.W. and J. Klerer, *Physical Chemistry of Surfaces.* Journal of The Electrochemical Society, 1977. **124**(5): p. 192C-192C.

55. Yasuda, T., T. Okuno, and H. Yasuda, *Contact Angle of Water on Polymer Surfaces.* Langmuir, 1994. **10**(7): p. 2435-2439.

56.   Sinha, P.K. and C.-Y. Wang, *Liquid water transport in a mixed-wet gas diffusion layer of a polymer electrolyte fuel cell.* Chemical Engineering Science, 2008. **63**(4): p. 1081-1091.

57.   Gostick, J.T., et al., *Capillary pressure and hydrophilic porosity in gas diffusion layers for polymer electrolyte fuel cells.* Journal of Power Sources, 2006. **156**(2): p. 375-387.

58.   Phillips, M. and A. Riddiford, *The specific free surface energy of paraffinic solids.* Journal of colloid and interface science, 1966. **22**(2): p. 149-157.

59.   Petke, F.D. and B.R. Ray, *Temperature dependence of contact angles of liquids on polymeric solids.* Journal of colloid and interface science, 1969. **31**(2): p. 216-227.

60.   Zettlemoyer, A.C., *Hydrophobic surfaces.* Journal of Colloid and Interface Science, 1968. **28**(3–4): p. 343-369.

61.   Fowkes, F.M. and W.D. Harkins, *The State of Monolayers Adsorbed at the Interface Solid—Aqueous Solution.* Journal of the American Chemical Society, 1940. **62**(12): p. 3377-3386.

62.   Gostick, J.T., et al., *Direct measurement of the capillary pressure characteristics of water–air–gas diffusion layer systems for PEM fuel cells.* Electrochemistry communications, 2008. **10**(10): p. 1520-1523.

63.   Kell, G.S., *Density, thermal expansivity, and compressibility of liquid water from 0.deg. to 150.deg.. Correlations and tables for atmospheric pressure and saturation reviewed and expressed on 1968 temperature scale.* Journal of Chemical & Engineering Data, 1975. **20**(1): p. 97-105.

64.   Yan, A., et al., *Controlling water contact angle on carbon surfaces from 5 deg to 167 deg.* Carbon, 2006. **44**(14): p. 3116-3120.

65.   Boyes, A. and A. Ponter, *Wettability of copper and polytetrafluoroethylene surfaces with water—the influence of environmental conditions.* Chemie Ingenieur Technik, 1973. **45**(21): p. 1250-1256.

66.   Petersen, P.B. and R.J. Saykally, *On the nature of ions at the liquid water surface.* Annu. Rev. Phys. Chem., 2006. **57**: p. 333-364.

67.   Boström, M., D.R.M. Williams, and B.W. Ninham, *Surface tension of electrolytes: specific ion effects explained by dispersion forces.* Langmuir, 2001. **17**(15): p. 4475-4478.

68.   Welzel, P.B., et al., *Influence of Aqueous Electrolytes on the Wetting Behavior of Hydrophobic Solid Polymers—Low-Rate Dynamic Liquid/Fluid Contact Angle Measurements Using Axisymmetric Drop Shape Analysis.* Journal of colloid and interface science, 2002. **251**(1): p. 101-108.

69.   Weissenborn, P.K., *Surface tension and bubble coalescence phenomena of aqueous solutions of electrolytes.* Langmuir, 1995. **11**(5): p. 1422.

70.   Hey, M.J., et al., *Surface tensions of aqueous solutions of some 1:1 electrolytes.* Journal of the Chemical Society, Faraday Transactions 1: Physical Chemistry in Condensed Phases, 1981. **77**(1): p. 123-128.

71.   Zhou, Z.A., et al., *Interaction of Ionic Species and Fine Solids with a Low Energy Hydrophobic Surface from Contact Angle Measurement.* Journal of Colloid and Interface Science, 1998. **204**(2): p. 342-349.

72.   Arbiter, N., et al., *Surface properties of hydrophobic solids*. 1964: Society of Mining Engineers of AIME.

Appendix A. Nomenclature

A.1. Variables and Parameters

P_C	Capillary Pressure	[Pa]
P_L	Liquid Pressure	[Pa]
P_G	Gas Pressure	[Pa]
r	Mean Pores Radius	[m]
n	Number of electrons transferred	
S_w	Water Saturation	[m^3 of water / m^3 of pore volume]
P_D	Differential Pressure	[Pa]
P_{ATM}	Atmospheric Pressure	[Pa]
h	Height	[m]
D	Diameter	[m]
V	Volume	[m^3]
T	Temperature	[C]
V_w	Volume of Water	[m^3]
V_P	Pore Volume	[m^3]
m_w	Mass of Water	[kg]

A.2. Greek Symbols

σ_{LG}	Liquid Gas Surface Tension
θ	Contact Angle
σ_{SL}	Solid Liquid Surface Tension
σ_{SG}	Solid Gas Surface Tension
μ	Micro
ρ	Density
δ	Thickness

θ_A	Advancing contact angle	
θ_R	Receding contact angle	
ε	Porosity	
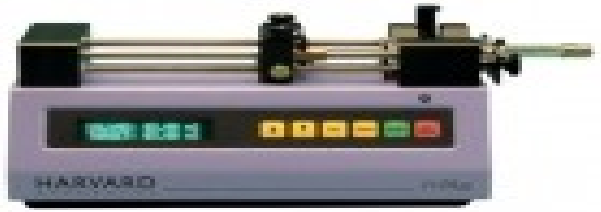
A.3. Physico-Chemical Constants

| F | Faraday Constant | $96487[C/mol]$ |

Appendix B. Instruments

B.1. Syringe Pump

Specifications	Picture
- Model: 11 Plus - Supplier: Harvard Apparatus - Pump Function: Infuse/ Withdrawal - Syringe size: Maximum 50 ml - Syringe Size: Minimum 0.5 µl - Communication: RS-232 - Price: 2188.00 $	

B.2. Oven

Specifications	Picture
- Model: DKN402/602/812/912 - Supplier: Yamato Scientific Co. Ltd, Japan - Temperature Range: Room Temp±10°C to 210°C - Type: Mechanical Convection - Thermal Accuracy: ±1°C - Price: 5300 $	

B.3. Pressure Sensors

B.3.1. Differential Pressure Sensor

Specifications	Picture
- Model: MMDWU10WV10K2B0T2A2S - Range: 0 to 2.5 KPa - Output : 0 to 10 Vdc - Serial No: 404355 - Supplier: Omega Engineering Inc. - Temperature Range : -18 to 93C - Thermal Accuracy : ± 0.8 - Price:1137.00$	

B.3.2. Absolute Pressure Sensor

Specifications	Picture
- Model : PX409-030A5V - Range : 0 to 30 - Serial No: 417796 - Supplier: Omega Engineering Inc. - Price: 525.00$	

B.4. Solenoid Valve

Specifications	Picture
- Part Identification No (PIN): 22Z1008NSCH - Type : 2 ways (usually closed) - Supplier : Peter Paul Electronics - Volt :120V - Watt : 7.7 - Orifice : 1/8" - Price: 90.00$	

B.5. Hydrophobic Membrane

Specifications	Picture
- Suppliers : Sartorious Stedium Biotech - Trade name : Satorius, 0.4µm PTFE# 11806-25 - Diameter : 25mm - Pore size: 0.45 µm - Maximum Operating Temp. : 85°C - Material : PTFE - Porosity : 70% - Price : $91.75	

B.6. Hydrophilic Membrane

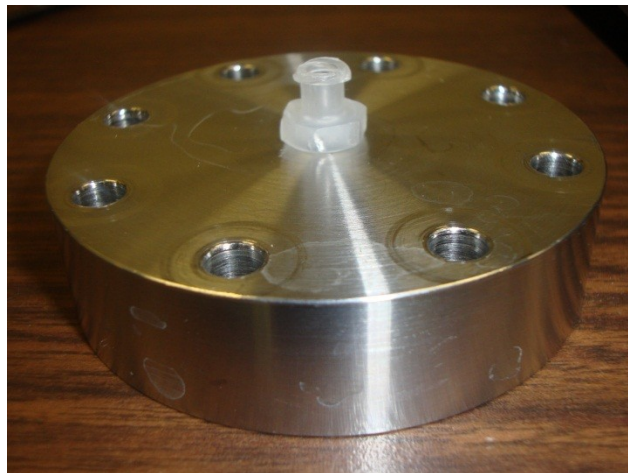| Specification	Picture
- Suppliers: Millipore - Trade name : Durapore membrane, PVDF - Diameter : 47 mm - Pore size: 0.22 μm - Maximum Operating Temp. : 85°C - Filter Code : GVWP - Porosity : 70% - Price : 147.00 $ Canadian/100 Pcs.	

B.7. Sample Holder

Picture 1: Bottom Plate

Picture 2: Middle plate viewed from bottom

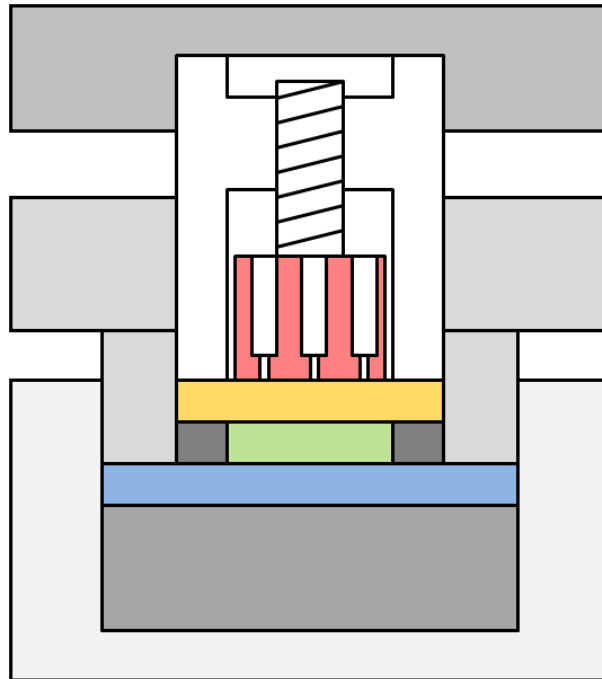**Picture 3: Top plate viewed from top**

Picture 4: Liquid distributor

Picture 5: Compressor cylinder
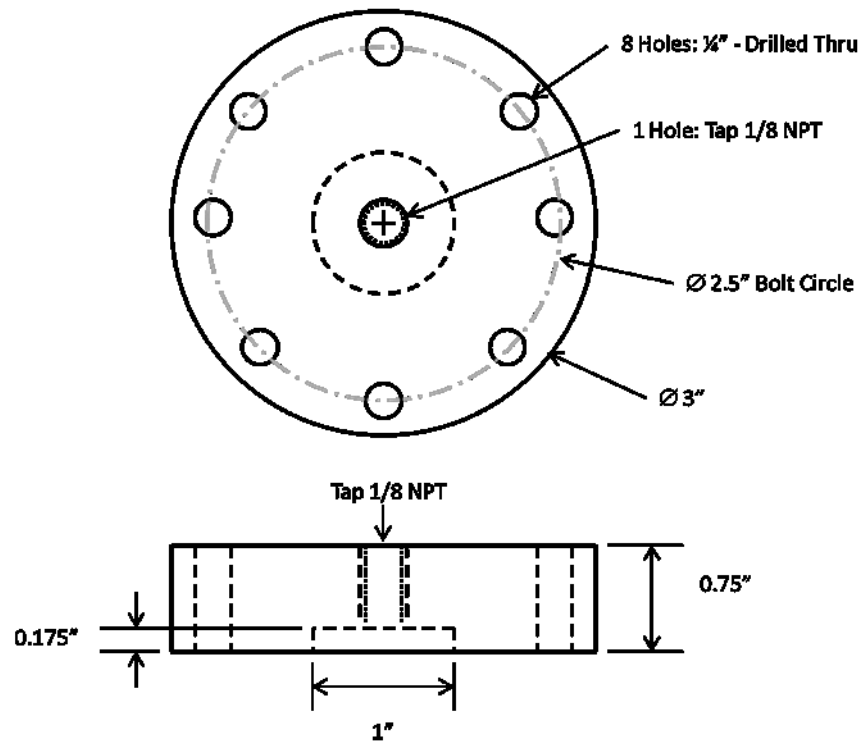
B.8.   Plug with hole arrangement

Picture 6: Sample holder highlighting Pug with holes arrangement.

Appendix C. Technical Drawing of Sample Holder

C.1. Top Plate

Top Plate

Material: 304 Stainless

8 Holes: ¼" - Drilled Thru

1 Hole: Tap 1/8 NPT

Ø 2.5" Bolt Circle

Ø 3"

Tap 1/8 NPT

0.75"

0.175"

1"

C.2. Compression Cylinder

Compression Cylinder 1

Material: 304 Stainless

Drill Thru and Tap: ¼-20

Channel for O-Ring

Ø 1"

Channel for O-Ring –
1/8" Cross-Section

1.25"

0.5"

Groove for O-Ring –
1/16" Cross-Section

0.750"
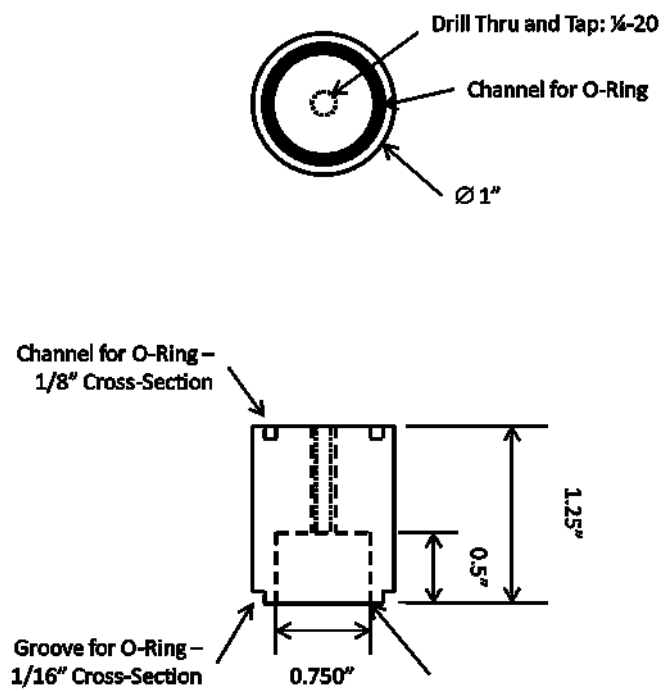
C.3. Water Distributor

Liquid Distributor

Material: 304 Stainless

$\varnothing 2.000''$ $\begin{matrix} +0.000 \\ -0.002 \end{matrix}$

13 Holes Total: 0.0127" - Drilled Thru
Note: Pilot holes inside bottom cavity
are acceptable

Drill ¾" Deep and Tap 10-32

$\varnothing 0.70''$ Hole Circle

$\varnothing 0.35''$ Hole Circle

Groove for O-ring –
1/8" Cross-Section,
ID > 1.85"

Mirror Finish, both sides

0.325"

0.25"

1.25"
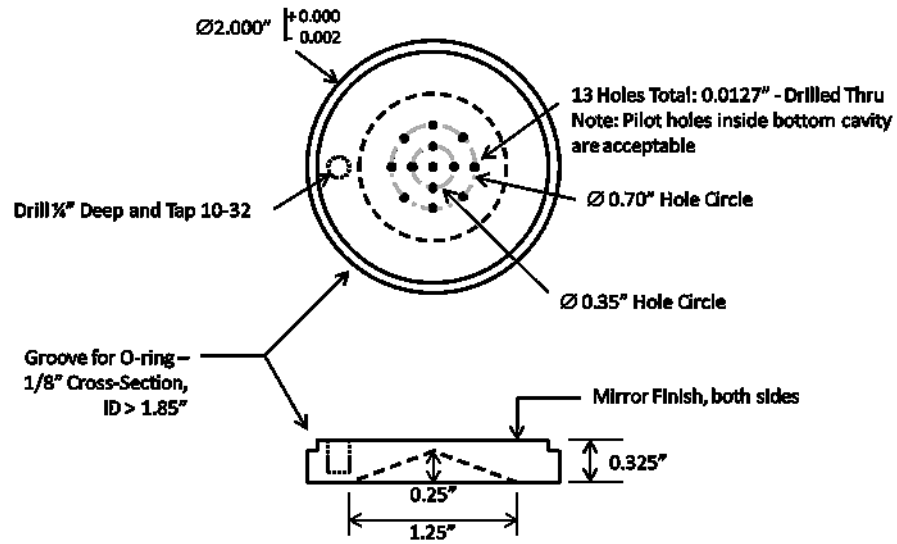
C.4. Middle Plate

Middle Plate 1

8 Holes: ¼" – Drilled Thru

$\varnothing 1" \begin{vmatrix} +0.000 \\ -0.004 \end{vmatrix}$

Ø 2.5" Bolt Circle

Ø 3"

0.75"

0.25"

Mirror Finish

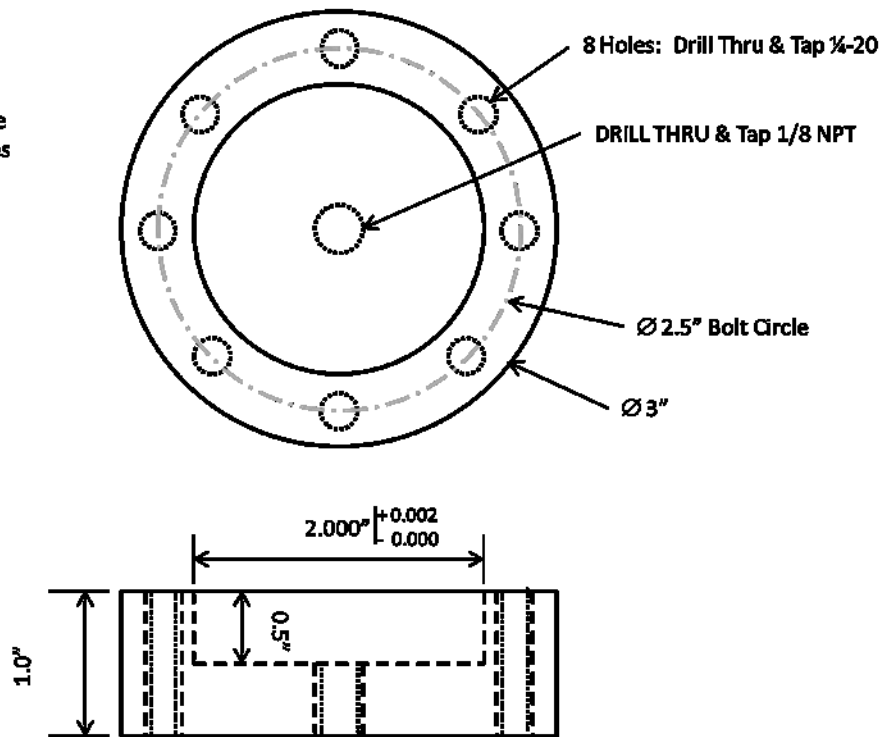2.000" $\begin{vmatrix} +0.000 \\ -0.004 \end{vmatrix}$
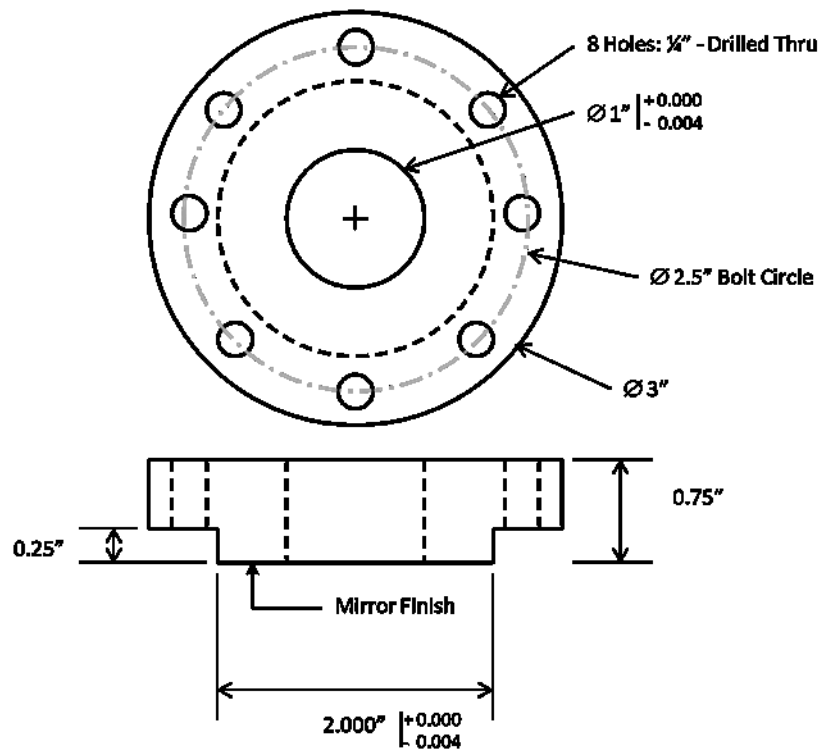
C.5. Bottom Plate
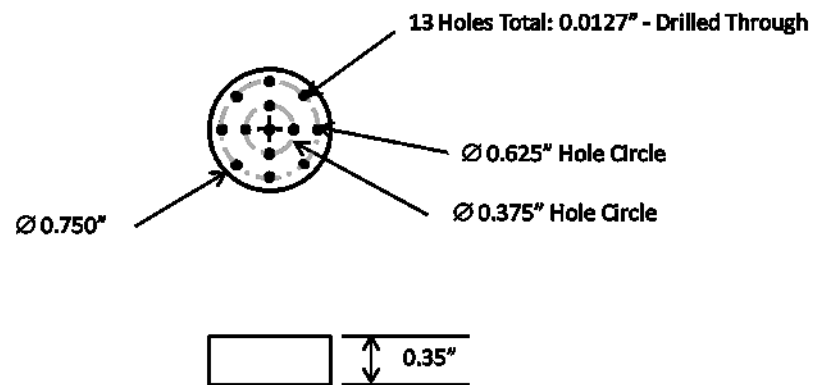
Bottom Plate

Material: 304 Stainless

Note: The **Liquid Distributor** part should form a sliding fit in the cavity of this plate. Please apply necessary tolerances to I.D. of cavity.

8 Holes: Drill Thru & Tap ¼-20

DRILL THRU & Tap 1/8 NPT

Ø 2.5" Bolt Circle

Ø 3"

2.000" $^{+0.002}_{-0.000}$

0.5"

1.0"

C.6. Gas distributor Plug

Gas Distributor Plate

Material: Teflon

13 Holes Total: 0.0127" - Drilled Through
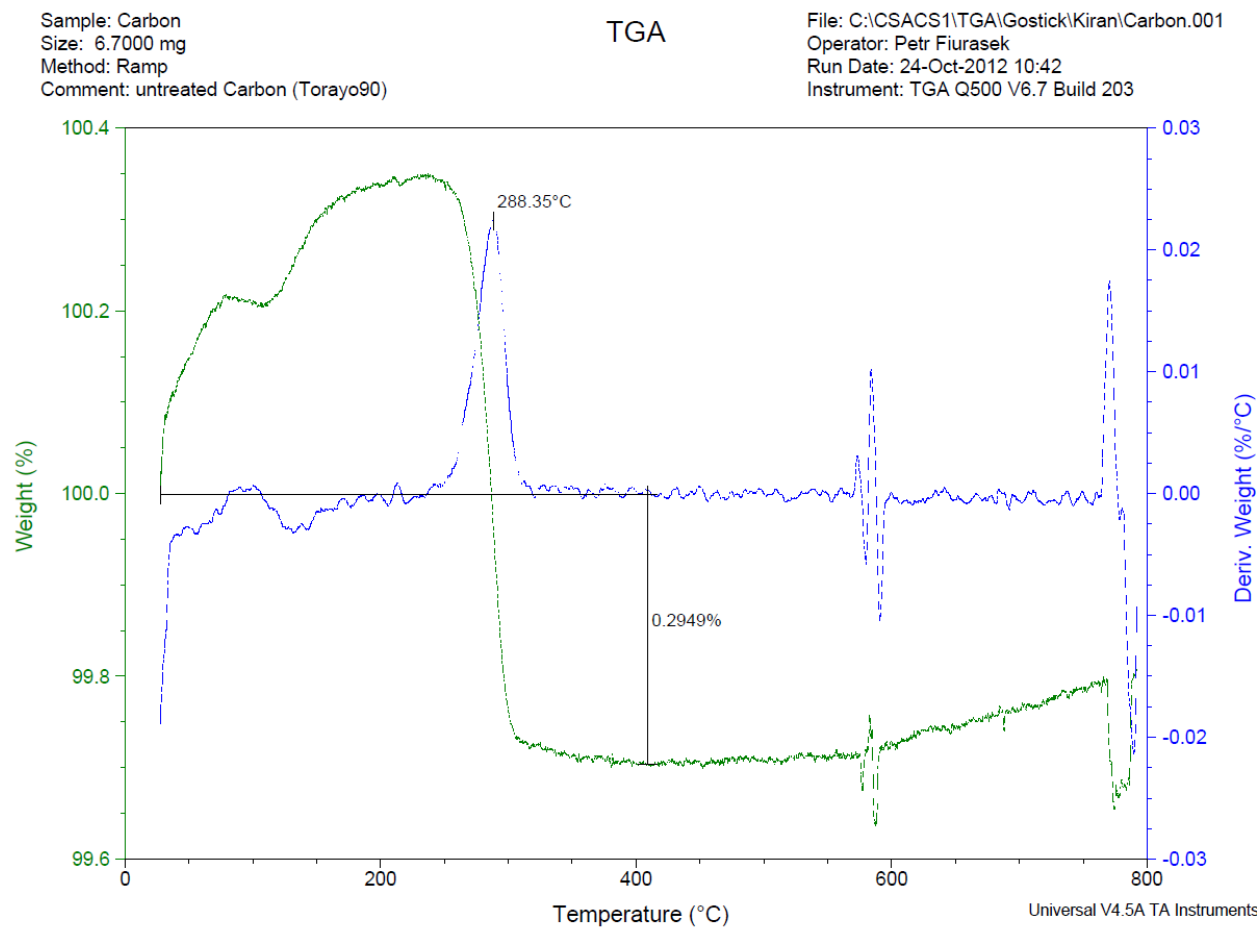
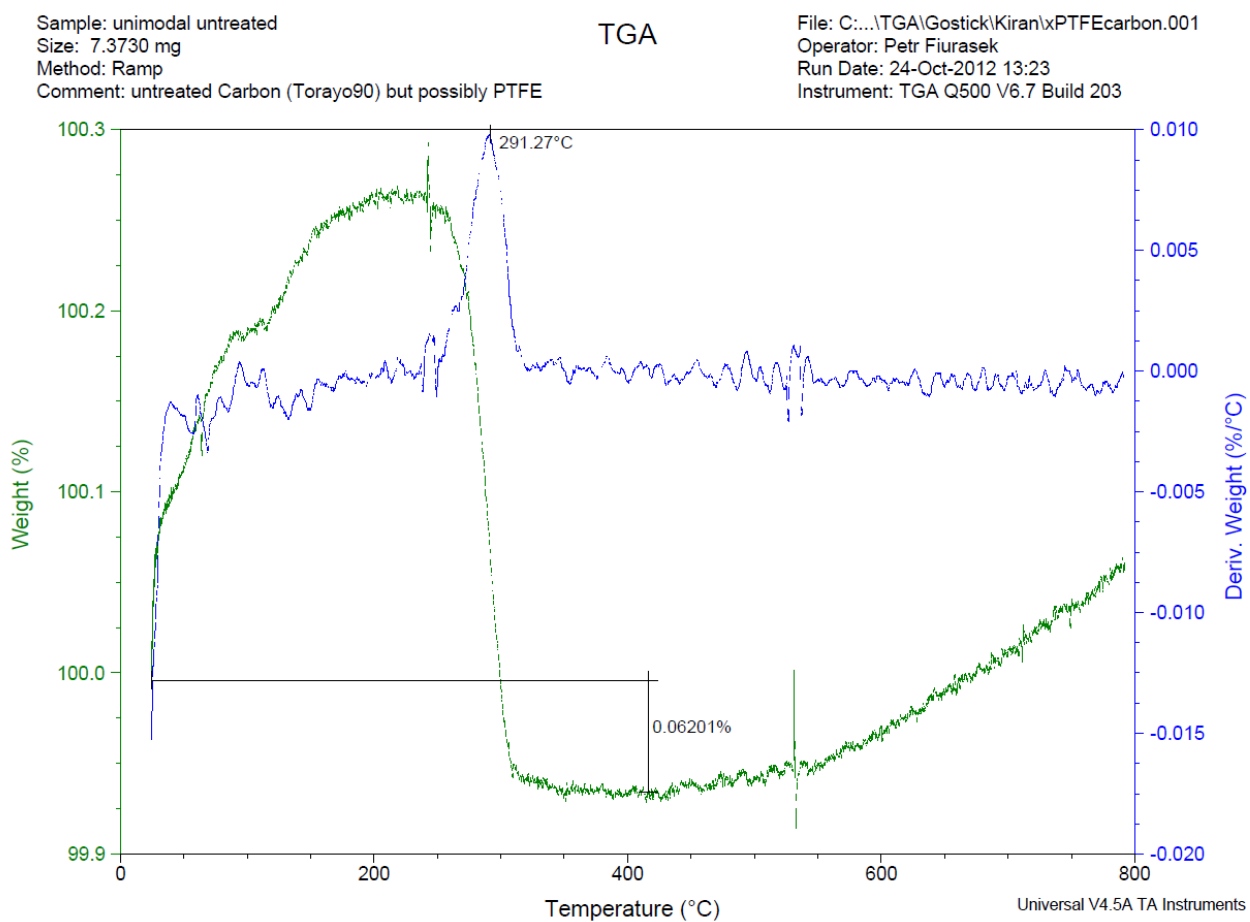Ø 0.625" Hole Circle

Ø 0.375" Hole Circle

Ø 0.750"

0.35"

Note: Hidden lines not shown for clarity

Appendix D. Thermo Gravimetric Analysis (TGA)

D.1. Toray 090b

D.2. Toray090 untreated (Industrial partner)

Sample: unimodal untreated
Size: 7.3730 mg
Method: Ramp
Comment: untreated Carbon (Torayo90) but possibly PTFE

TGA

File: C:...\TGA\Gostick\Kiran\xPTFEcarbon.001
Operator: Petr Fiurasek
Run Date: 24-Oct-2012 13:23
Instrument: TGA Q500 V6.7 Build 203

291.27°C

0.06201%

Universal V4.5A TA Instruments

D.3. Toray090 10%PTFE

9.643%

Universal V4.5A TA Instrument

87
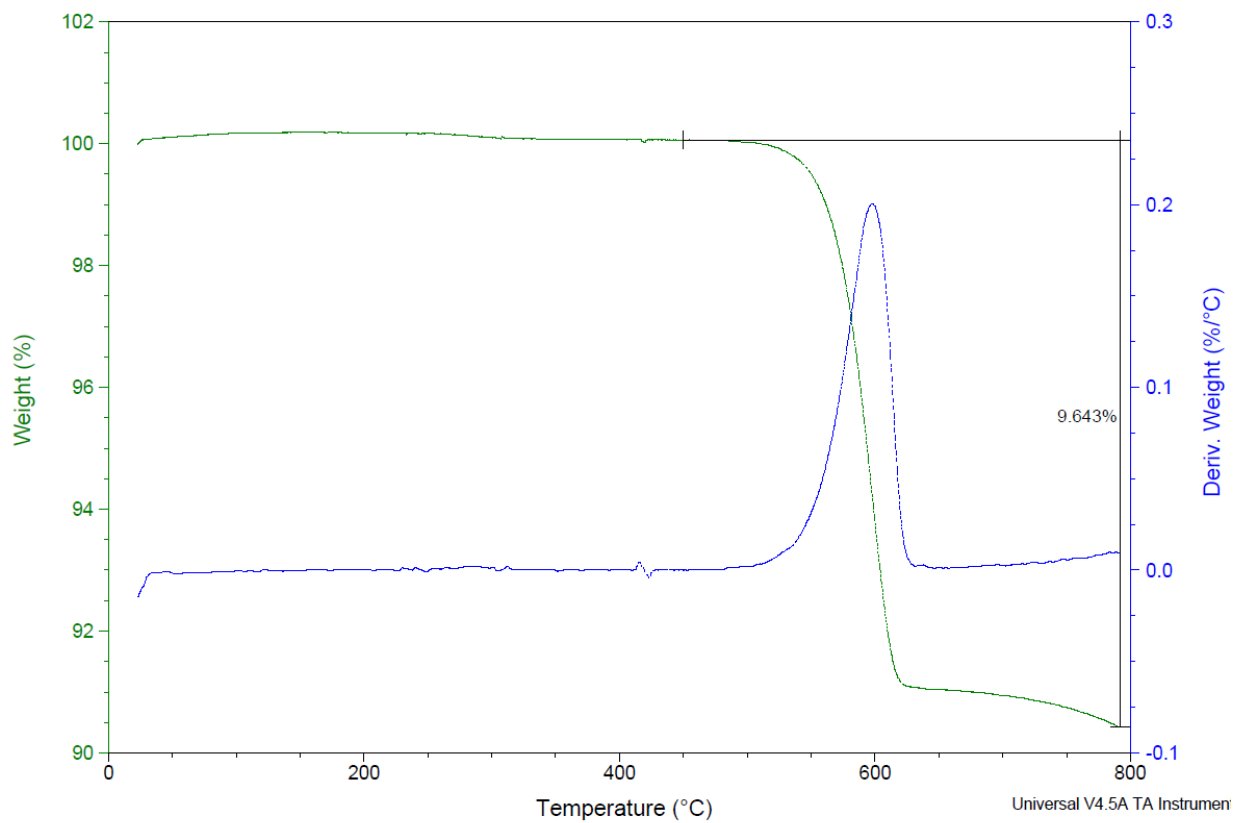
Appendix E. Filament Analog Model

The filament analog model converts the solid volume of the many short fibers in the actual material to a single long filament of the same diameter.   The extent of thermal expansion in both the longitudinal and radial direction on this filament can be calculated with temperature. This model is utilised to determine the percentage variation of porosity of GDL sample due to the thermal expansion of graphite over the range of 60°C which is the actual range of temperature utilised during experiment. As shown in Table 2, the percentage variation of porosity of a typical GDL sample is only 0.05%.

Table 2 : Calculation showing percentage variation of porosity of GDL sample at temperature range of 60K.

Particulars	Formulas	Symbols	Values	Units
Thickness of GDL sample		t	0.000272	m
Diameter of GDL sample		D	0.001905	m
Total Body Volume	$(Pi*D^2/4)*t$	V_B	7.75262E-10	m^3
Porosity		ε	0.74	
Total Solid Volume	$V_B(1-\varepsilon)$	V_S	2.01568E-10	m^3
Filament Diameter		f_d	0.00001	m
Length of Filament of volume V_s	$V_S/(Pi/4*D^2)$	L	2.56644648	m
Temperature coefficient of graphite		K	7.90E-06	m/mK
Temperature gradient		DT	60	K
New length after expansion	$L*K*DT$	L'	1.22E-03	m
New Diameter after expansion	f_d*K*DT	f_d'	4.74E-09	m
New Solid volume after expansion	$(pi/4*(f_d +f_d')^2*(L+L'))$	V'	2.0186E-10	m^3
Porosity after expansion	$1-V_b/V'$	ε'	0.739630105	
Percentage Variation in Porosity	$((\varepsilon-\varepsilon')/\varepsilon)*100$		0.05	%